

NUCLEAR DATA AND MEASUREMENTS SERIES

ANL/NDM-100

**The Energy Dependence of the Optical-Model Potential
for Fast-Neutron Scattering from Bismuth**

by

A.B. Smith, P.T. Guenther, and R.D. Lawson

May 1987

**ARGONNE NATIONAL LABORATORY,
ARGONNE, ILLINOIS 60439, U.S.A.**

NUCLEAR DATA AND MEASUREMENTS SERIES

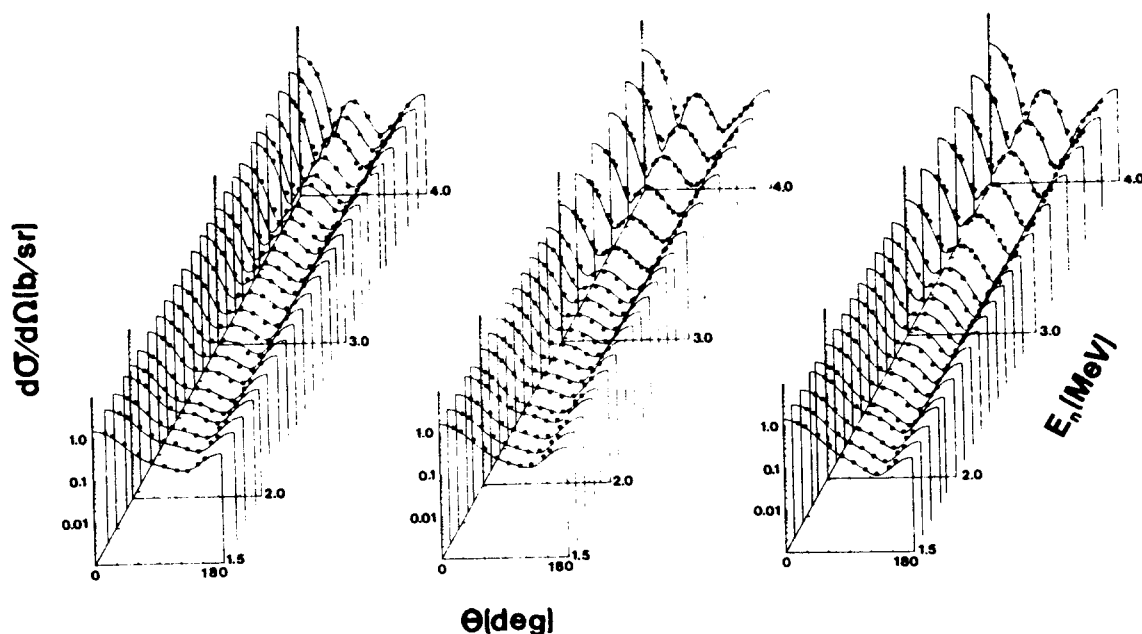
ANL/NDM-100

THE ENERGY DEPENDENCE OF THE OPTICAL-MODEL POTENTIAL FOR
FAST-NEUTRON SCATTERING FROM BISMUTH

BY

A. B. Smith, P. T. Guenther and R. D. Lawson

May 1987



ARGONNE NATIONAL LABORATORY, ARGONNE, ILLINOIS

Operated by THE UNIVERSITY OF CHICAGO

for the U. S. DEPARTMENT OF ENERGY

under Contract W-31-109-Eng-38

Argonne National Laboratory, with facilities in the states of Illinois and Idaho, is owned by the United States government, and operated by The University of Chicago under the provisions of a contract with the Department of Energy.

DISCLAIMER

This report was prepared as an account of work sponsored by an agency of the United States Government. Neither the United States Government nor any agency thereof, nor any of their employees, makes any warranty, express or implied, or assumes any legal liability or responsibility for the accuracy, completeness, or usefulness of any information, apparatus, product, or process disclosed, or represents that its use would not infringe privately owned rights. Reference herein to any specific commercial product, process, or service by trade name, trademark, manufacturer, or otherwise, does not necessarily constitute or imply its endorsement, recommendation, or favoring by the United States Government or any agency thereof. The views and opinions of authors expressed herein do not necessarily state or reflect those of the United States Government or any agency thereof.

ANL/NDM-100

THE ENERGY DEPENDENCE OF THE OPTICAL-MODEL POTENTIAL FOR FAST-
NEUTRON SCATTERING FROM BISMUTH*

by

A. B. Smith, P. T. Guenther and R. D. Lawson

May 1987

Keywords:

NUCLEAR REACTIONS $^{209}\text{Bi}(n,n)$, $E_n = 4.5 - 10.0$ MeV,
Measured $\sigma(E,\theta)$; Optical-statistical model inter-
pretation.

Applied Physics Division
Argonne National Laboratory
9700 South Cass Avenue
Argonne, IL 60439
USA

*Work supported by the U.S. Department of Energy, Basic Energy Science Programs under contract W-31-109-ENG-38.

NUCLEAR DATA AND MEASUREMENTS SERIES

The Nuclear Data and Measurements Series presents results of studies in the field of microscopic nuclear data. The primary objective is the dissemination of information in the comprehensive form required for nuclear technology applications. This Series is devoted to: a) measured microscopic nuclear parameters, b) experimental techniques and facilities employed in measurements, c) the analysis, correlation and interpretation of nuclear data, and d) the evaluation of nuclear data. Contributions to this Series are reviewed to assure technical competence and, unless otherwise stated, the contents can be formally referenced. This Series does not supplant formal journal publication but it does provide the more extensive information required for technological applications (e.g., tabulated numerical data) in a timely manner.

Copies on microfiche can be obtained by contacting:

National Technical Information Service
U.S. Department of Commerce
5285 Port Royal Road
Springfield, Virginia 22161
U.S.A.

INFORMATION ABOUT OTHER ISSUES IN THE ANL/NDM SERIES

A list of titles and authors for reports ANL/NDM-1 through ANL/NDM-50 can be obtained by referring to any report of this Series numbered ANL/NDM-51 through ANL/NDM-76. Requests for a complete list of titles or for copies of previous reports should be directed to:

Section Secretary
Applied Nuclear Physics Section
Applied Physics Division
Building 316
Argonne National Laboratory
9700 South Cass Avenue
Argonne, Illinois 60439
U.S.A.

- ANL/NDM-51 A. Smith, P. Guenther, D. Smith and J. Whalen, *Measured and Evaluated Cross Sections of Elemental Bismuth*, April 1980.
- ANL/NDM-52 P. Guenther, A. Smith and J. Whalen, *Neutron Total and Scattering Cross Sections of ${}^6\text{Li}$ in the Few-MeV Region*, February 1980.
- ANL/NDM-53 James W. Meadows and Donald L. Smith, *Neutron-source Investigations in Support of the Cross-section Program at the Argonne Fast-neutron Generator*, May 1980.
- ANL/NDM-54 A.B. Smith, P.T. Guenther and J.F. Whalen, *The Nonelastic-scattering Cross Sections of Elemental Nickel*, June 1980.

- ANL/NDM-55 M.M. Bretscher and D.L. Smith, *Thermal-neutron Calibration of a Tritium Extraction Facility using the ${}^6\text{Li}(n,t){}^4\text{He}/\text{Au}(n,\gamma){}^{198}\text{Au}$ Cross-section Ratio for Standardization*, August 1980.
- ANL/NDM-56 P.T. Guenther, A.B. Smith and J.F. Whalen, *Fast-neutron Interaction with ${}^{182}\text{W}$, ${}^{184}\text{W}$ and ${}^{186}\text{W}$* , December 1980.
- ANL/NDM-57 Peter T. Guenther, Alan B. Smith and James F. Whalen, *The Total, Elastic- and Inelastic-scattering Fast-neutron Cross Sections of Natural Chromium*, January 1981.
- ANL/NDM-58 W.P. Poenitz, *Review of Measurement Techniques for the Neutron-capture Process*, August 1981.
- ANL/NDM-59 Wolfgang P. Poenitz, *Review of the Importance of the Neutron-capture Process in Fission Reactors*, July 1981.
- ANL/NDM-60 James W. Meadows and Donald L. Smith, *Gamma-ray Detector Calibration Methods Utilized in the Argonne FNG Group Activation Cross-section Measurement Program*, April 1984.
- ANL/NDM-61 Carl Budtz-Joergensen, Peter T. Guenther, Alan B. Smith and James F. Whalen, *Fast-neutron Total and Scattering Cross Sections of ${}^{58}\text{Ni}$* , September 1981.
- ANL/NDM-62 Donald L. Smith, *Covariance Matrices and Applications to the Field of Nuclear Data*, November 1981.
- ANL/NDM-63 Alan B. Smith and Peter T. Guenther, *On Neutron Inelastic-scattering Cross Sections of ${}^{232}\text{Th}$, ${}^{233}\text{U}$, ${}^{235}\text{U}$, ${}^{238}\text{U}$, ${}^{239}\text{U}$ and ${}^{239}\text{Pu}$ and ${}^{240}\text{Pu}$* , January 1982.

- ANL/NDM-64 James W. Meadows and Carl Budtz-Joergensen, *The Fission-fragment Angular Distributions and Total Kinetic Energies for $^{235}\text{U}(n,f)$ from 0.18 to 8.83 MeV*, January 1982.
- ANL/NDM-65 Alan B. Smith and Peter T. Guenther, *Note on the Elastic Scattering of Several-MeV Neutrons from Elemental Calcium*, March 1982.
- ANL/NDM-66 Alan B. Smith and Peter T. Guenther, *Fast-neutron Scattering Cross Sections of Elemental Silver*, May 1982.
- ANL/NDM-67 Donald L. Smith, *Non-evaluation Applications for Covariance Matrices*, July 1982.
- ANL/NDM-68 Alan B. Smith, Peter T. Guenther and James F. Whalen, *Fast-neutron Total and Scattering Cross Sections of ^{103}Rh* , July 1982.
- ANL/NDM-69 Alan B. Smith and Peter T. Guenther, *Fast-neutron Scattering Cross Sections of Elemental Zirconium*, December 1982.
- ANL/NDM-70 Alan B. Smith, Peter T. Guenther and James F. Whalen, *Fast-neutron Total and Scattering Cross Sections of Niobium*, July 1982.
- ANL/NDM-71 Alan B. Smith, Peter T. Guenther and James F. Whalen, *Fast-neutron Total and Scattering Cross Sections of Elemental Palladium*, June 1982.
- ANL/NDM-72 Alan B. Smith and Peter T. Guenther, *Fast-neutron Scattering from Elemental Cadmium*, July 1982.

- ANL/NDM-73 C. Budtz-Joergensen, Peter T. Guenther and Alan B. Smith, *Fast-neutron Elastic-scattering Cross Sections of Elemental Tin*, July 1982.
- ANL/NDM-74 Wolfgang Poenitz, Alan B. Smith and Robert Howerton, *Evaluation of the ^{238}U Neutron Total Cross Section*, December 1982.
- ANL/NDM-75 A.B. Smith, P.T. Guenther and J.F. Whalen, *Neutron Total and Scattering Cross Sections of Elemental Antimony*, September 1982.
- ANL/NDM-76 Alan B. Smith and Peter T. Guenther, *Scattering of Fast Neutrons from Elemental Molybdenum*, November 1982.
- ANL/NDM-77 Donald L. Smith, *A Least-squares Method for Deriving Reaction Differential Cross Section Information from Measurements Performed in Diverse Neutron Fields*, November 1982.
- ANL/NDM-78 A.B. Smith, P.T. Guenther and J.F. Whalen, *Fast-neutron Total and Elastic-scattering Cross Sections of Elemental Indium*, November 1982.
- ANL/NDM-79 C. Budtz-Joergensen, P. Guenther, A. Smith and J. Whalen, *Few-MeV Neutrons Incident on Yttrium*, June 1983.
- ANL/NDM-80 W.P. Poenitz and J.F. Whalen, *Neutron Total Cross Section Measurements in the Energy Region from 47 keV to 20 MeV*, July 1983.
- ANL/NDM-81 D.L. Smith and P.T. Guenther, *Covariances for Neutron Cross Sections Calculated Using a Regional Model Based on Elemental-model Fits to Experimental Data*, November 1983.

- ANL/NDM-82 D.L. Smith, *Reaction Differential Cross Sections from the Least-squares Unfolding of Ratio Data Measured in Diverse Neutrons Fields*, January 1984.
- ANL/NDM-83 J.W. Meadows, *The Fission Cross Sections of Some Thorium, Uranium, Neptunium and Plutonium Isotopes Relative to ^{235}U* , October 1983.
- ANL/NDM-84 W.P. Poenitz and J.W. Meadows, *^{235}U and ^{239}Pu Sample-mass Determinations and Intercomparisons*, November 1983.
- ANL/NDM-85 D.L. Smith, J.W. Meadows and I. Kanno, *Measurement of the $^{51}\text{V}(n,p)^{51}\text{Ti}$ Reaction Cross Section from Threshold to 9.3 MeV*, June 1984.
- ANL/NDM-86 I. Kanno, J.W. Meadows and D.L. Smith, *Energy-differential Cross-section Measurement for the $^{51}\text{V}(n,\alpha)^{48}\text{Sc}$ Reaction*, July 1984.
- ANL/NDM-87 D.L. Smith, J.W. Meadows, M.M. Bretscher and S.A. Cox, *Cross-section Measurement for the $^7\text{Li}(n,n't)^4\text{He}$ Reaction at 14.74 MeV*, September 1984.
- ANL/NDM-88 A.B. Smith, D.L. Smith and R.J. Howerton, *An Evaluated Nuclear Data File for Niobium*, March 1985.
- ANL/NDM-89 Bernard P. Evain, Donald L. Smith and Paul Lucchese, *Compilation and Evaluation of 14-MeV Neutron-activation Cross Sections for Nuclear Technology Applications: Set I*, April 1985.
- ANL/NDM-90 D.L. Smith, J.W. Meadows and P.T. Guenther, *Fast-neutron-spectrum Measurements for the Thick-target $^9\text{Be}(d,n)^{10}\text{B}$ Reaction at $E_d = 7$ MeV*, April 1985.

- ANL/NDM-91 A.B. Smith, P.T. Guenther and R.D. Lawson, *On the Energy Dependence of the Optical Model of Neutron Scattering from Niobium*, May 1985.
- ANL/NDM-92 Donald L. Smith, *Nuclear Data Uncertainties (Vol.-I): Basic Concepts of Probability*, April 1986.
- ANL/NDM-93 D.L. Smith, J.W. Meadows and M.M. Bretscher, *Integral Cross-section Measurements for ${}^7\text{Li}(n,n't){}^4\text{He}$, ${}^{27}\text{Al}(n,p){}^{27}\text{Mg}$, ${}^{27}\text{Al}(n,\alpha){}^{24}\text{Na}$, ${}^{58}\text{Ni}(n,p){}^{58}\text{Co}$ and ${}^{60}\text{Ni}(n,p){}^{60}\text{Co}$ Relative to ${}^{238}\text{U}$ Neutron Fission in the Thick-target ${}^9\text{Be}(d,n){}^{10}\text{B}$ Spectrum at $E_d = 7$ MeV*, October 1985.
- ANL/NDM-94 A.B. Smith, D.L. Smith, P. Rousset, R.D. Lawson and R.J. Howerton, *Evaluated Neutronic Data File for Yttrium*, January 1986.
- ANL/NDM-95 Donald L. Smith and James W. Meadows, *A Facility for High-intensity Neutron Irradiations Using Thick-target Sources at the Argonne Fast-neutron Generator*, May 1986.
- ANL/NDM-96 M. Sugimoto, A.B. Smith and P.T. Guenther, *Ratio of the Prompt-Fission-Neutron Spectrum of Plutonium 239 to that of Uranium 235*, September 1986.
- ANL/NDM-97 J.W. Meadows, *The Fission Cross Sections of ${}^{230}\text{Th}$, ${}^{232}\text{Th}$, ${}^{233}\text{U}$, ${}^{234}\text{U}$, ${}^{236}\text{U}$, ${}^{238}\text{U}$, ${}^{237}\text{Np}$, ${}^{239}\text{Pu}$ and ${}^{242}\text{Pu}$ Relative to ${}^{235}\text{U}$ at 14.74 MeV Neutron Energy*, December 1986.
- ANL/NDM-98 J.W. Meadows, *The Fission Cross Section Ratios And Error Analysis For Ten Thorium, Uranium, Neptunium and Plutonium Isotopes at 14.74 MeV Neutron Energy*, March 1987.

ANL/NDM-99 D.L. Smith, *Some Comments on the Effects of Long-Range
Correlations in Covariance Matrices for Nuclear Data*,
March 1987.

TABLE OF CONTENTS

| | Page |
|---|------|
| Preface | x |
| Abstract. | 1 |
| I. Introduction | 3 |
| II. Experimental Methods | 5 |
| III. Experimental Results | 6 |
| IV. Optical-Model Interpretations | 11 |
| V. Discussion | 21 |
| VI. Summary. | 36 |
| Acknowledgments | 39 |
| References | 40 |

PREFACE

This issue marks the centennial contribution to the ANL/NDM report series from Argonne National Laboratory. This series is produced within the Applied Nuclear Physics Section of the Applied Physics Division at Argonne. The first report in this series appeared in July 1973. For those of us who have been involved in both contributing to this series and producing it, this issue represents an occasion for both celebration and reflection.

This series was conceived to meet a need which existed at that time, and one which we feel still exists to this day, namely for a quality medium for reporting the results of nuclear data research in sufficient detail so that interested readers will have in their possession all the information they require to fully comprehend and/or implement the numerical data provided or concepts elaborated therein. Judging from the favorable feedback we have received over the years, including very encouraging responses to our periodic requests for "subscription" renewals, and many new requests received for inclusion on the "NDM" mailing list, it is our firm conviction that this series has fulfilled the role we envisioned for it nearly 14 years ago. In practice this series has involved many more individuals beyond our group membership. Through the years, as the result of numerous collaborations which this group has enjoyed, authors from a number of other laboratories have shared the bylines of reports in this series. We feel, therefore, that in some measure this series has played a significant role within the larger nuclear data community beyond the confines of this laboratory.

The range of material which has been addressed in this series over the years has indeed been very broad. Expositions involving engineering details, experimental physical measurements, nuclear modeling, statistical methods, comprehensive reviews, etc., have graced the pages of reports in this series on many occasions. The general format of the series, while having survived numerous transitions in its mechanical production (from mechanical typewriters to computer-based wordprocessors), has changed rather little since the inception. The procedures relating to detailed peer review and meticulous attention to the production of the documents, in order to insure survival of a minimal numbers of errors, have also been preserved. In short, this series has benefited from the continuity of purpose and a commitment to excellence which was decreed from the very beginning.

For those readers who have been regular recipients of issues in this series under "subscription", we hope that these reports have come to form an important element of your personal library of nuclear data information. New or casual readers who wish to be

added to our list of "subscribers" are invited to contact us as indicated elsewhere in this report. This series has existed to serve the nuclear data community. As we enter our second "century", we pledge our efforts to a continuation of this service.

The Research Staff of the Applied Nuclear Physics Section, Applied Physics Division, Argonne National Laboratory, May 18, 1987.

ANL/NDM-100

THE ENERGY DEPENDENCE OF THE OPTICAL-MODEL POTENTIAL
FOR FAST-NEUTRON SCATTERING FROM BISMUTH*

by

A. B. Smith, P. T. Guenther and R. D. Lawson

May 1987

Applied Physics Division
Argonne National Laboratory
9700 South Cass Avenue
Argonne, Illinois 60439
USA

ABSTRACT

Neutron differential-elastic-scattering cross sections of bismuth were measured at ≈ 0.5 MeV intervals from ≈ 4.5 to 10.0 MeV. At each incident energy ≥ 40 differential values were obtained, distributed between $\approx 18^\circ$ and 160° . The measured data were combined with lower-energy results previously reported from this laboratory, and others available in the literature, to provide a detailed data base extending from ≈ 1.5 to 10.0 MeV. This data base was interpreted in terms of the conventional optical-statistical model and also a model inclusive of the surface-peaked real potential predicted by the dispersion relation. Particular attention was given to the energy dependence of the volume-integral-per-nucleon of the real potential, J_v , to see if there was evidence of the Fermi Surface Anomaly. In the range 3.0 to 10.0 MeV the present data indicate that dJ_v/dE is essentially constant, with a relatively large negative value of -6.0 to -9.0 fm³, depending on the model used in the analysis. Below 3.0 MeV, there is some evidence for a decrease in the magnitude of dJ_v/dE . However, the effect is very small and it is only when this trend is combined with considerations of the J_v values needed to give correct

bound-state energies that evidence for the Fermi Surface Anomaly emerges. J_v and the geometry of the optical potentials found for ^{209}Bi become equal to those needed to explain the high-energy ^{208}Pb data at about 10.0 MeV. Since dJ_v/dE for the latter is smaller in magnitude than for ^{209}Bi , a change in dJ_v/dE is clearly indicated near 10.0 MeV. This may effect the extrapolation of higher-energy and charged-particle potentials into the lower-energy neutron domain.

* This work supported by the U. S. Department of Energy, Basic Energy Science Programs, under the contract W-31-109-Eng-38.

I. INTRODUCTION

It has been known for many years that the observed level spacings and binding energies of the single-particle and single-hole states in ^{208}Pb can be predicted by the use of a static Woods-Saxon potential (1). This means that the effective mass, m^* , of a valence nucleon is nearly equal to its free mass, m , and this in turn implies that $dV/dE \approx 0$ near the Fermi surface (2), an effect known as the Fermi Surface Anomaly. Mahaux and Ngô (3) have made detailed studies of the polarization and correlation contributions to the optical-model potential for this doubly-closed-shell nucleus. They predict that below about 6.0 MeV the real potential has a highly non-linear energy dependence, and that dV/dE becomes zero near $E = 4.0$ MeV. Charged-particle-scattering sheds little light on this phenomena since the energies of interest are at or below the coulomb barrier. However, an analysis of the lower-energy neutron elastic-scattering angular distributions, using the spherical optical-statistical model, should show these effects. Because ^{208}Pb is a doubly-closed-shell nucleus, fluctuations in the compound-nucleus cross section are large and can strongly affect the analysis of lower-energy neutron scattering data. On the other hand, the neighboring element bismuth is monoisotopic, ^{209}Bi , and has a high density of states near the neutron binding energy. Therefore, it offers the opportunity for study of energy-averaged cross sections, consistent with the concept of the optical model, down to fairly low energies without undue perturbations from fluctuation effects.

There have been several comprehensive studies of elastic-neutron scattering from ^{209}Bi from several-hundred keV to approximately 4.0 MeV (4, 5, 6). However, except for the 7.0 MeV data of Zafiratos et al. (7) and the ≈ 6.0 , 7.0 and 8.0 MeV distributions of Holmqvist and Wiedling (8), there was little information available above 4.0 MeV until the recent work of Annand et al. (9), who reported detailed measurements in the 4.0 to 7.0 MeV range. In this paper we report twelve new neutron elastic-scattering angular distributions, distributed in energy from 4.5 to 10.0 MeV at intervals of approximately 0.5 MeV. These new data were combined with the lower-energy results of references 5 and 6 to provide a detailed data base, extending over the energy range 1.5 to 10.0 MeV, for neutron scattering from ^{209}Bi . This data base was then analyzed using the spherical optical-statistical-model theory to determine the best

parameterization of the model, and to examine the energy dependence of J_v , the volume-integral-per-nucleon of the real potential, over the energy range 1.5 to 10.0 MeV.

In Section II we briefly discuss the experimental methods used to obtain the data, and the experimental results are presented in Section III. Section IV contains a description of two variants of the optical model used in the interpretation of the data: first, the conventional optical-statistical model in which the real potential was taken to have the Woods-Saxon form; and second, the model in which a surface-peaked component predicted by the dispersion relationship (2) is added to this well. In Section V the properties of the ^{209}Bi optical-model potential are discussed and evidence for the Fermi Surface Anomaly is presented. Also, in this section it is shown that a combined interpretation of the ^{209}Bi and ^{208}Pb data leads to the conclusion that dJ_v/dE changes its magnitude near $E = 10.0$ MeV. Finally, in Section VI the findings of this work are summarized.

The behavior of dJ_v/dE near 10.0 MeV for neutron scattering has applied implications. In particular, it suggests that the extrapolation of high-energy neutron or charged-particle models to provide parameters to be used in predicting low-energy cross sections of applied importance should be undertaken with some discretion.

II. EXPERIMENTAL METHODS

The time-of-flight methods used in the present measurements have been extensively employed at the Argonne Tandem Dynamitron. Since they have been described in detail on a number of occasions (10, 11, 12), only a brief outline is given here.

The measurement samples were solid cylinders 2 cm in diameter by 2 cm long. The neutrons were incident on their lateral surfaces. The bismuth sample was cast of chemically-pure metal and machined to size. The polyethylene reference sample was machined from commercially available material. Sample densities were determined to better than 0.01% using conventional measurement techniques.

The $D(d,n)^3\text{He}$ reaction (13) was used as the neutron source throughout the measurements. The mean neutron energies were determined to ≈ 25 keV by control of the incident-deuteron beam. The deuteron-gas target was contained in a cell ≈ 3.5 cm long, at pressures resulting in neutron energy spreads at the sample of ≈ 100 -200 keV, decreasing with increasing energy. The deuteron beam was pulsed at a 2 MHz repetition rate, with a burst duration of ≈ 1 nsec. The scattering samples were placed 15-18 cm from the source at a zero-degree reaction angle.

The measurements were made using the Argonne 10-channel time-of-flight apparatus (12). The time spectra of neutrons scattered over flight paths of ≈ 503 cm were concurrently measured at ten scattering angles. The angular setting of the entire apparatus was varied several times to obtain differential cross sections at 40 or more angles at each incident energy. Two additional time channels provided redundant monitoring of the neutron-source intensity. Relative detector sensitivities were determined using the well-known spectrum of neutrons emitted from a spontaneously-fissioning ^{252}Cf source, as described in reference 14. The absolute sensitivity of the detector system was determined relative to the $H(n,n)$ scattering standard (15) using polyethylene (CH_2) as the hydrogenous scattering sample. The observed scattering distributions from bismuth and from hydrogen were corrected for multiple-event, angular-resolution, and incident-beam-attenuation effects using analytical and Monte-Carlo methods (16).

III. EXPERIMENTAL RESULTS

Differential neutron-elastic-scattering distributions were measured for twelve incident-neutron energies between 4.5 and 10.0 MeV, at approximately 0.5-MeV intervals. Each distribution consisted of at least 40 differential cross sections (≈ 100 at some energies) distributed over the angular range $\approx 18^\circ$ to 160° . The scattered-neutron energy resolution was sufficient to separate the elastic-scattered neutron group from all known inelastic-scattering components. Some of the latter data were reduced to cross sections, but since they are not germane to the present considerations they will be reported elsewhere (17). Throughout the measurements, differential elastic-scattering cross sections of carbon were also concurrently determined at each energy in order to verify the fidelity of the measurement system relative to well-known carbon values (15).

Considerable attention was given to the definition of experimental uncertainties as they can significantly influence the subsequent model fitting. At most scattering angles the statistical uncertainties (foreground and background) were relatively small ($\leq 1\%$), but they could be considerably larger at the deep minima of the distributions. The neutron detector calibrations, based upon the $H(n,n)$ cross sections, were believed known to $\leq 3\%$. This conclusion was supported by the consistency of results obtained many months apart with essentially independent instrument calibrations. The relative neutron-scattering angles were optically established to $\leq 0.1^\circ$. The absolute calibration of this angular system was determined at each measurement period by observing forward-angle neutron scattering both left and right of the apparent center line, and the true angular zero is believed known to $\leq 0.25^\circ$. However, for heavy nuclei the elastic-scattering cross section varies rapidly with angle. Thus even this small angular uncertainty, when folded into the strongly angular-dependent cross sections, can make a major contribution to the experimental uncertainty at some angles. The multiple-event-correction procedures introduced additional uncertainties, generally $\leq 1\%$, but larger near the minima of the distributions. There were systematic uncertainties associated with sample masses and the $H(n,n)$ reference cross sections; both were relatively small ($\leq 1\%$). These various sources of experimental error were combined in quadrature to obtain the total experimental uncertainty. In addition, a minimum uncertainty of 2 mb/sr was assumed as representative of unknown error sources and general detection sensitivity. The

latter contribution can be significant at the minima of the distributions. Finally, it should be pointed out that the measurement method involved the use of ten essentially-independent detection systems, resulting in a considerable degree of redundancy that made possible the verification of a number of the above uncertainty estimates.

The experimental results, with their uncertainties, are shown in Fig. 1. Prior directly-comparable results are remarkably sparse and are largely summarized in Fig. 2. The results of reference 8 are reasonably consistent with the present values at ≈ 7 and 8 MeV, but are less so at ≈ 6 MeV. The ≈ 6 MeV results of reference 18 differ at some angles from the present values, and the same is true for the ≈ 7 -MeV results of reference 19. However, the 7-MeV results of reference 7 are in excellent agreement with those of the present work. More recently, Annand et al. (9) have reported results in the 4- to 7-MeV range and, judging from their figures, their values seem to be consistent with those of the present work. The present experimental results nicely extrapolate to the lower-energy (≤ 4.0 MeV) values previously reported from this laboratory (5) and those of Olsson et al. (6), as illustrated in Fig. 3.

In view of the above considerations, it is reasonable to base an interpretation of the interaction of ≤ 10 -MeV neutrons with ^{209}Bi upon the present data, extended to lower energies by the use of the results of references 5 and 6.

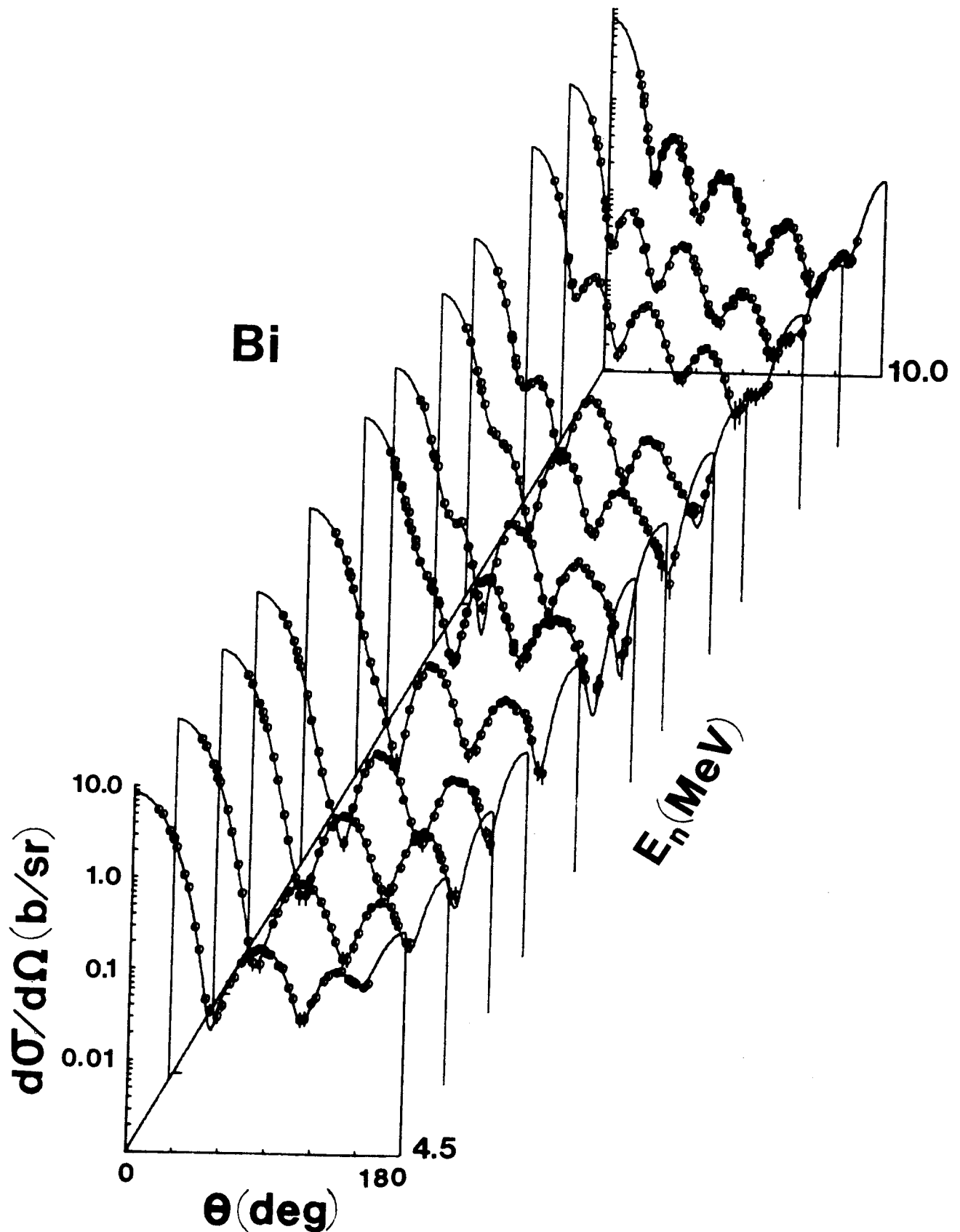


Fig. 1. Differential elastic neutron scattering from bismuth as a function of laboratory scattering angle and neutron energy. The present results are noted by data symbols. The curves are eyeguides.

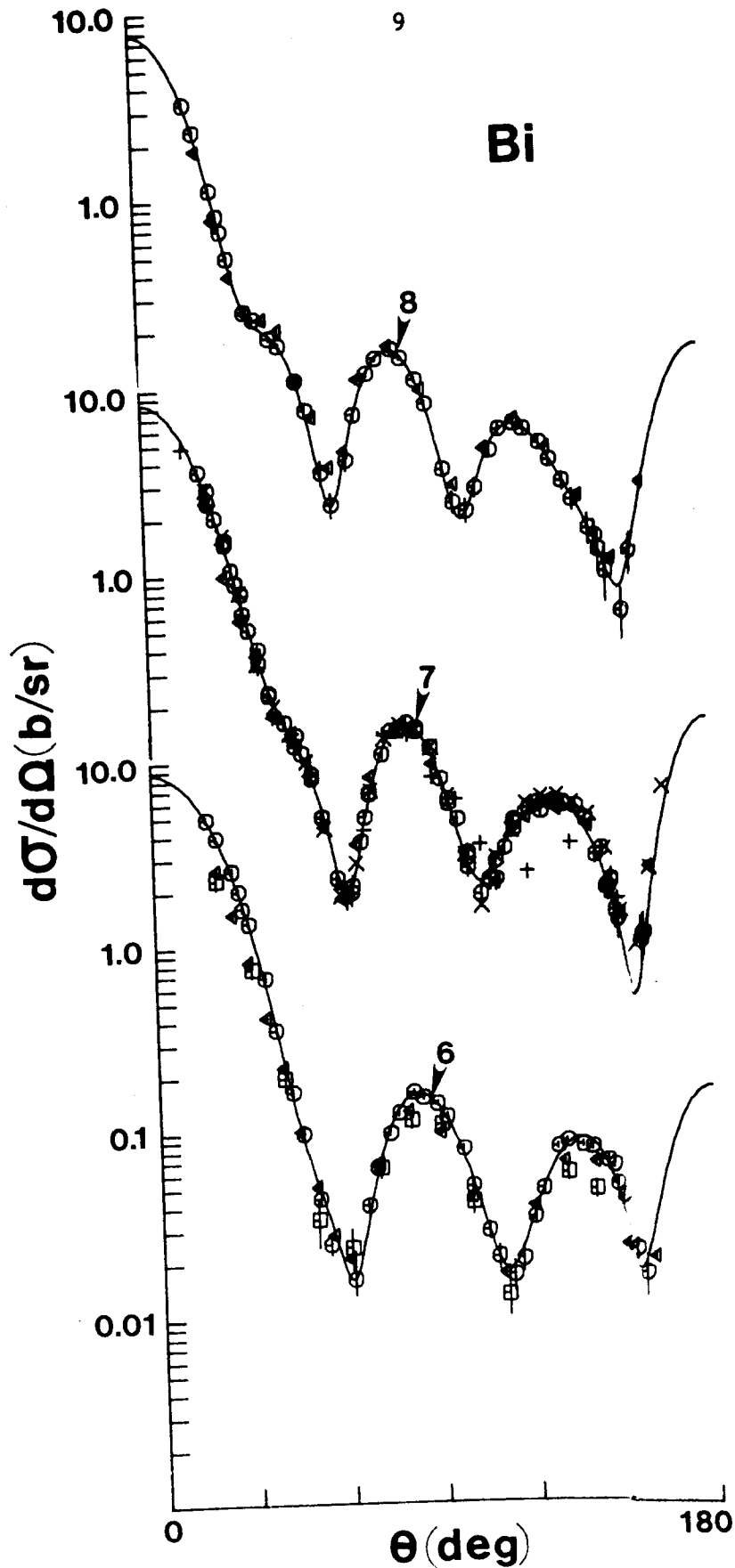


Fig. 2. Comparison of the present experimental results (O) with those reported in the literature (x = ref. 7, \triangleleft = ref. 8, \square = ref. 18, and + = ref. 19). Approximate neutron energies in MeV are noted numerically. Curves are eyeguides. Scattering angles and neutron energies are given in the laboratory system.

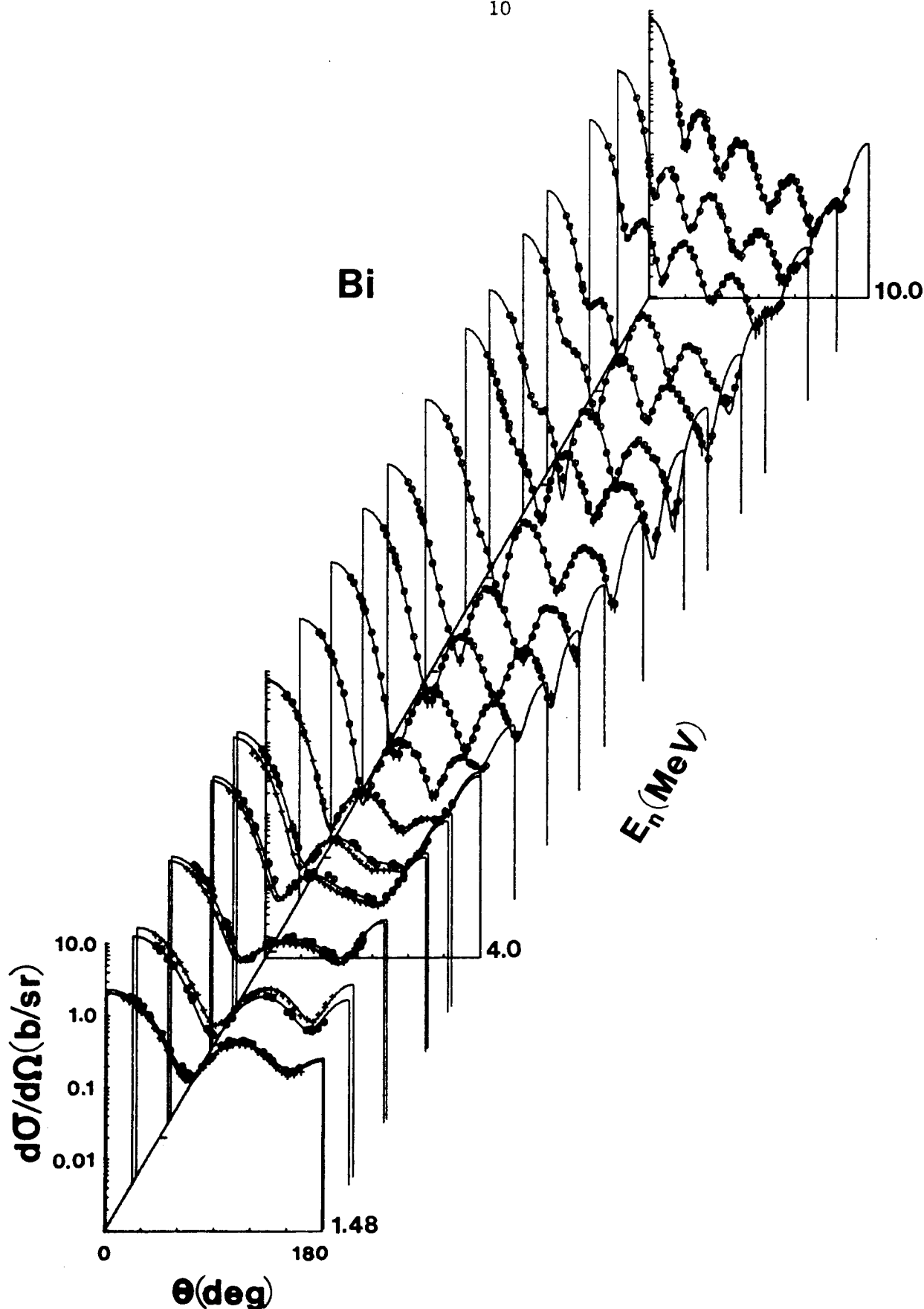


Fig. 3. The present experimental results for $E \geq 4.5$ MeV, together with the lower-energy ($E \leq 4.0$ MeV) values previously reported from this laboratory (o) and as given in ref. 6 (+). For clarity, values from refs. 5 and 6 are shown only at ≈ 0.5 MeV intervals. Curves are eyeguides. Scattering angles and neutron energies are in the laboratory system.

IV. OPTICAL-MODEL INTERPRETATIONS

The optical-model interpretations were based upon three sets of differential-elastic-scattering data: i) the present results extending from 4.5 to 10.0 MeV, ii) the 1.5 to 4.0 MeV results reported earlier from this laboratory (5), and iii) the ≈ 1.5 to 4.0 MeV results reported by Olsson et al. (6). Specification of the experimental uncertainties is essential for quantitative interpretation, and thus the present work gave considerable attention to their definition, as described in Section III. The earlier work of reference 5 was carried out with an applied objective and does not have the accuracy of the present results, but it is in good agreement with the values of reference 6. Furthermore, the experimental uncertainties are reasonably well defined. The uncertainties associated with the work of reference 6 are not as clearly specified, either in the journal paper or in the underlying laboratory report. Therefore, a simple assumption of equal percentage uncertainties for all datum values was made. This assumption can distort the parameters resulting from the interpretations. An additional data set extending from 0.3 to 1.5 MeV has been reported by some of the present authors (4). It was not used in these analyses as it involves relatively low energies where the assumptions underlying the use of the optical model are not valid due to evident fluctuations. There are a few other differential elastic-scattering distributions in the 1.5 to 10.0 MeV energy range reported in the literature and available from the files of the National Nuclear Data Center, Brookhaven National Laboratory. Some of this additional information was not available in numerical form and thus could not be used in these present interpretations. In the few cases where numerical results were available they tended to support the above three primary data sets, as illustrated in Fig. 2.

A. Conventional Optical Model

Initially, a conventional spherical optical-statistical model was assumed, consisting of a Woods-Saxon real potential, a Woods-Saxon-derivative imaginary well, and a Thomas spin-orbit interaction (20). Below ≈ 6.5 MeV compound-nucleus effects were a concern and were calculated using the Hauser-Feshbach formula (21), as modified for width-fluctuation and correlation corrections by Moldauer (22). Discrete states were included in the calculations to an excitation energy of ≈ 3.2 MeV, using the spin and parity assignments of Lederer and Shirley (23). Above this energy, the target level density was computed from the formula

$$\rho(E, J) = \frac{(2J + 1)}{2\sigma^2 T} \exp((E - E_0)/T) \exp(-(J + 1/2)^2/2\sigma^2), \quad (1)$$

where J is the angular momentum of the continuum target level and E_0 , T and σ are parameters. No values for these parameters are

given by Gilbert and Cameron (24) for ^{209}Bi . However, all the bismuth isotopes they considered have about the same value for the spin-cut-off parameter, σ , which we took equal to 4.4. In the incident-neutron energy range 3.2-6.5 MeV, compound elastic scattering contributes very significantly to the magnitude of the differential cross section at the back-angle minima. Consequently, with σ fixed, we adjusted E_0 and T so as to best reproduce these cross-section minima. The resulting level-density parameters were

$$\begin{aligned} E_0 &= 0.1 \text{ MeV} \\ T &= 1.15 \text{ MeV} \\ \sigma &= 4.4. \end{aligned} \quad (2)$$

The derivation of the optical-model potential from the measured values was based upon χ^2 fitting procedures, minimizing the quantity

$$\chi^2 = \sum_i \left[\frac{\sigma_{\text{exp}}(\theta_i) - \sigma_{\text{cal}}(\theta_i)}{\delta\sigma_{\text{exp}}(\theta_i)} \right]^2, \quad (3)$$

where $\delta\sigma_{\text{exp}}(\theta_i)$ is the experimental uncertainty associated with the elastic-scattering cross section, $\sigma_{\text{exp}}(\theta_i)$, of the data base and $\sigma_{\text{cal}}(\theta_i)$ is its calculated value. The fitting procedures started with a subjective examination of the spin-orbit potential, using distributions in the 9- to 10-MeV range where the observables are more sensitive to this potential. Six-parameter fits were made (concurrently varying real and imaginary strengths, radii and diffusenesses), using a mesh of spin-orbit potential strengths and geometries. From these considerations, the parameters characterizing the spin-orbit interaction were taken to be

$$\begin{aligned} V_{\text{so}} &= 5.22 \text{ MeV} \\ r_{\text{so}} &= 1.005 \text{ fm} \\ a_{\text{so}} &= 0.65 \text{ fm}, \end{aligned} \quad (4)$$

and these values were held constant throughout the remainder of the fitting. In all cases the nuclear radii of the potentials are $R_i = r_i A^{1/3}$. The possibility of a contribution from volume absorption at these higher energies was also examined, but no evidence for this interaction was found.

With the fixed spin-orbit strength, each of the distributions of the entire data base was fitted using six adjustable parameters, with particular attention to the values of the new 4.5 to 10.0 MeV measurements. The results of this fitting indicated a relatively stable imaginary radius, so that parameter was fixed to the average value of $r_w = 1.3102$ fm for subsequent five-parameter fits to the entire data base. The latter indicated an energy-dependent real radius given by $r_v = (1.36 - 0.0175 \times E(\text{MeV}))$ fm. The fitting procedure was then repeated using four parameters, and the resulting imaginary diffuseness was selected as the most stable of the remaining geometric parameters. It displayed a strong energy dependence given by $a_w = (0.05 + 0.055 \times E(\text{MeV}))$ fm. Proceeding in a similar manner through a three-parameter fitting process, the real diffuseness $a_v = (0.54 + 0.02 \times E(\text{MeV}))$ fm was obtained, where the energy dependence is slight, if present at all. Thus the final geometric parameters were taken to be

$$\begin{aligned}
 r_v &= (1.36 - 0.0175 \times E) \text{ fm} \\
 r_w &= 1.3102 \text{ fm} \\
 a_v &= (0.54 + 0.02 \times E) \text{ fm} \\
 a_w &= (0.05 + 0.055 \times E) \text{ fm},
 \end{aligned}
 \tag{5}$$

where E is the incident energy in MeV. Using this geometry, two-parameter fits were carried out in which the real and imaginary potential strengths were varied. A very good description of the data base was then obtained, as illustrated in Fig. 4. Despite the fact that the geometries of Eq. 5 were chosen mainly from the consideration of the new 4.5 to 10.0 MeV data, this figure shows that an excellent fit to the older 1.5 to 4.0 MeV results can be obtained with the same geometric parameters. Moreover, although not shown, these parameters can be extrapolated to give a reasonable description of the very low energy (0.3 - 1.5 MeV) data of reference 4. The resulting real and imaginary potential strengths, expressed as

volume-integrals-per-nucleon ($J_i = \frac{4\pi}{A} \int V_i(r) r^2 dr$), are shown in Fig. 5. If one considers only the new 4.5 to 10.0 MeV data,

the J_i values have a linear dependence on bombarding energy, E (in MeV), given by

$$\begin{aligned} J_v &= ((459.78 \pm 2.41) - (9.58 \pm 0.32) \times E) \quad \text{MeV-fm}^3 \\ J_w &= ((33.87 \pm 2.70) + (1.05 \pm 0.37) \times E) \quad \text{MeV-fm}^3, \end{aligned} \quad (6)$$

where the errors in the coefficients are almost exactly anticorrelated. In deducing these uncertainties a constant percentage error for each of the twelve values of J_v (J_w) was

assumed, and this percentage adjusted to give χ^2 per degree of freedom the value unity in each case. The values of Eqs. 6 are illustrated by the solid lines shown in Fig. 5. It appears that below ≈ 3.0 MeV, Eq. 6 tends to over-estimate the value of J_v obtained from the optical-model fits. This point is discussed further in the next section.

B. Surface Real Potential

The real optical-model potential is related to the imaginary interaction through the dispersion relation (2)

$$V(r, E) = V_{ws}(r, E) + \frac{P}{\pi} \int_{-\infty}^{+\infty} \frac{W(r, E') dE'}{(E - E')}, \quad (7)$$

where "P" stands for the principal-value integral, and $V_{ws}(r, E)$ is the Hartree-Fock potential which is taken to have the Woods-Saxon shape. This relation results in a surface-peaked addition to the real potential with a magnitude given by the integral of Eq. 7. Because the geometrical factors in $W(r, E')$ are energy dependent, it is more convenient to find the magnitude of this added potential from considerations involving $J_w(E')$.

The quantity

$$\lambda(E) = \left[\frac{P}{\pi} \int_{-\infty}^{+\infty} \frac{J_w(E') dE'}{E - E'} \right] / J_w(E) \quad (8)$$

is the factor by which $W(r, E)$ must be multiplied to give the surfaced-peaked contribution to the real potential (25). In evaluating the principal-value integral it has been assumed that J_w is symmetric about the Fermi energy (taken to be $E_F = -5.65$

MeV) and, in the energy range $2E_F \leq E' \leq 0$, is proportional to $(E - E_F)^2$ (26). In the range $0 \leq E' \leq 10.09$ MeV,

$$J_w = 30.93 + 1.37 \times E', \quad (9)$$

which is the best linear fit to all of the data points shown in Fig. 5. For the $10.09 \leq E' \leq 49.34$ MeV range, the surfaced-peaked imaginary potential of Walter and Guss (27) was used. The upper end of the energy range was dictated by the fact that the Walter-Guss potential goes to zero at that value of E' . The lower end, 10.09 MeV, was chosen to make $J_w(E')$ continuous, and, in addition, the function was made continuous at $E' = 0$. The resulting values of $\lambda(E)$ are shown in Fig. 6A.

The data were refitted including this surface-peaked real potential. The level-density parameters and the spin-orbit interaction were held fixed with the values of Eqs. 2 and 4, respectively. In a manner analogous to that described in Section IV-A, the geometric parameters of the real and imaginary potentials were deduced to be

$$\begin{aligned} r_v &= (1.28 - 0.007 \times E) \text{ fm} \\ r_w &= 1.3022 \text{ fm} \\ a_v &= 0.68 \text{ fm} \\ a_w &= (0.119 + 0.043 \times E) \text{ fm}, \end{aligned} \quad (10)$$

where E is the laboratory neutron bombarding energy in MeV. The value of r_w is essentially identical to that obtained with the conventional model. On the other hand, since a surface-peaked potential whose strength, as shown in Fig. 6A, decreases with increasing energy has been added, slower energy variation of r_v than found in Section IV-A would be anticipated. Moreover, r_v in this case should be smaller at low energies than the value given by the conventional model, but the two quantities should approach each other in the 9.0 MeV region where $\lambda(E)$ goes to zero. Comparison of Eqs. 5 and 10 shows these expectations to be borne out. The imaginary diffuseness again has a rapid energy variation, whereas a_v for the real potential can be taken to be energy independent in this case. Using these geometric factors, two-parameter fits were made and again a good description of the data was obtained, as illustrated in Fig. 7. Qualitatively, the description is similar to that obtained with the conventional model, Fig. 4, but close inspection of Fig. 7 indicates some

improvement in the description, and this is supported by generally smaller χ^2 values resulting from this fitting.

The values obtained for the volume-integrals-per-nucleon of the imaginary interaction and the real Woods-Saxon potential are shown in Figs. 6B and 6C, respectively. If one restricts oneself to the new 4.5 to 10.0 MeV data, a best fit to these values gives

$$\begin{aligned} J_{ws} &= ((422.41 \pm 2.46) - (4.83 \pm 0.33) \times E) \text{ MeV-fm}^3 \\ J_w &= ((31.03 \pm 2.48) + (1.41 \pm 0.34) \times E) \text{ MeV-fm}^3, \end{aligned} \quad (11)$$

where, again, E is the laboratory bombarding energy in MeV and the uncertainties in the coefficients were determined in the manner described in the discussion of Eq. 6. Considering the uncertainties in the coefficients, the form of J_w is quite similar to that obtained with the conventional model, Eq. 6. The parameters describing the variation of J_{ws} with energy cannot be compared directly with the values of J_v given in Eq. 6 because J_{ws} is the volume-integral-per-nucleon of only the Woods-Saxon part of the real potential. The quantity comparable to J_v is the sum of J_{ws} and $\lambda(E)J_w$, and this will be discussed later.

Because the geometry and strength of the imaginary potential is changed slightly from the values given in Section IV-A, the magnitude of the principal-value integral, Eq. 8, also changes. Thus, in order to do the calculations in a self-consistent manner, $\lambda(E)$ must be recalculated using the new form of J_w , and the fitting redone with this new magnitude of the added surface real potential. The new values of $\lambda(E)$ were calculated and fits performed at several energies. The results obtained were so close to the values given in the initial iteration that the more comprehensive self-consistent calculation was deemed unnecessary.

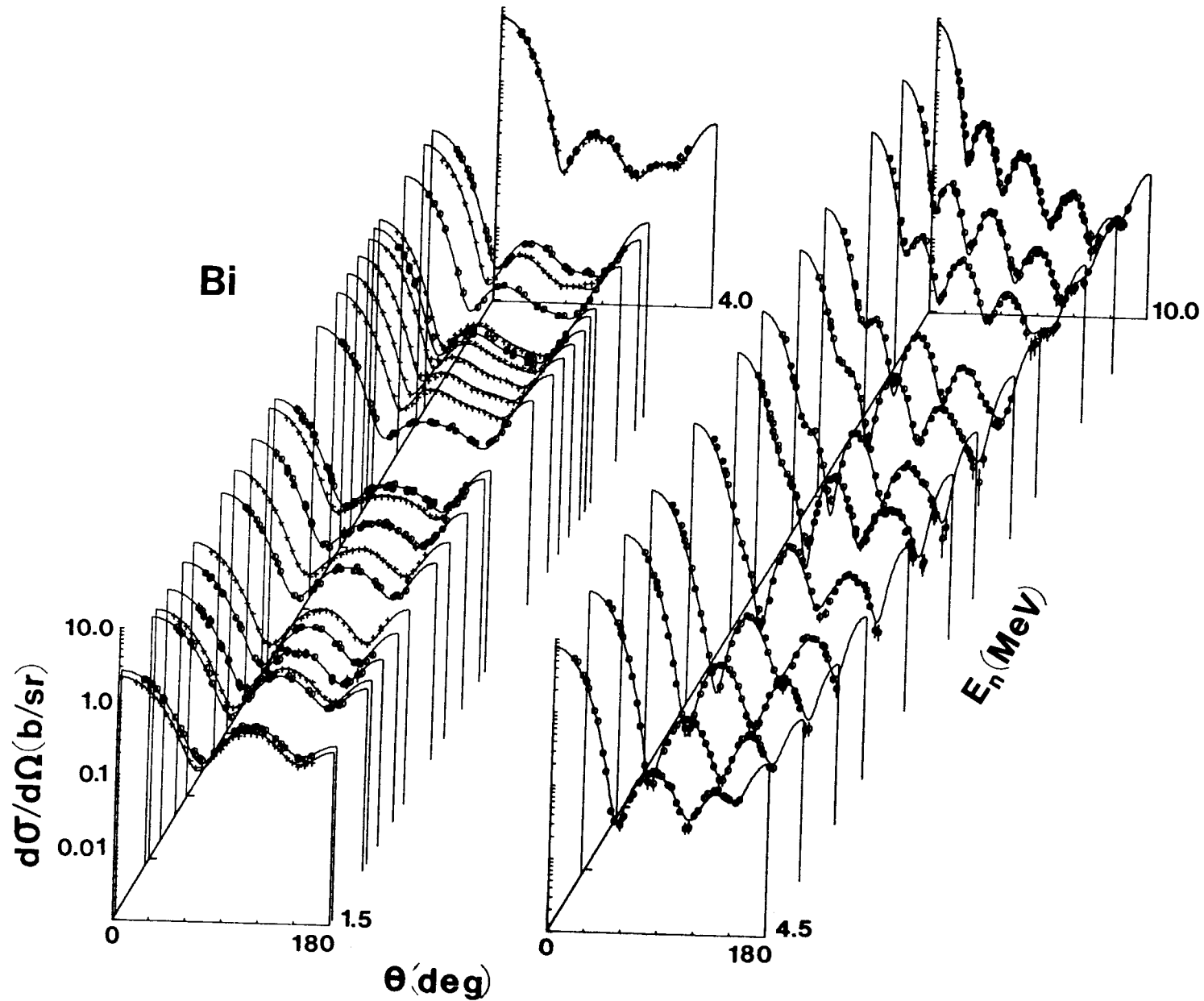


Fig. 4. Comparison of measured values ("o" indicating the present work and that of ref. 5, and "+" that of ref. 6) and the calculated results (curves) obtained using the conventional optical model, Sec. IV-A of the text.

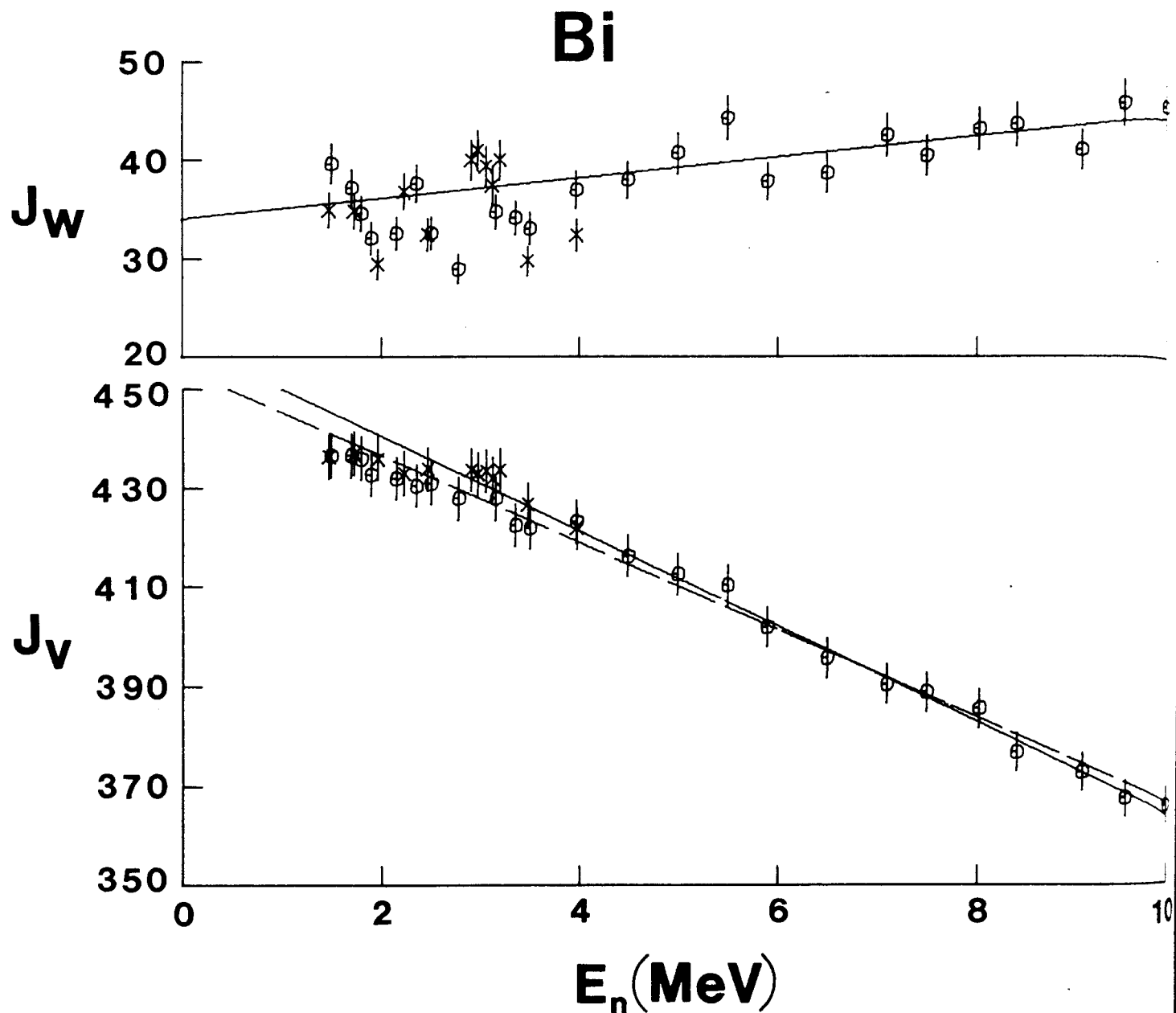


Fig. 5. The volume-integral-per-nucleon of the imaginary interaction, J_w , and the real potential, J_v , (in $\text{MeV}\cdot\text{fm}^3$) resulting from the conventional optical-model fit to the data, described in Sec. IV-A. The solid lines represent the fit to these volume integrals, Eq. 6, when only the 4.5 to 10.0 MeV data are used. The broken line in the J_v figure shows the fit when all J_v values are considered, Eq. 13. The "o" symbols indicated values derived from the present measurements and those of ref. 5, and "x" those derived from the experimental values of ref. 6. Here, and throughout the figures of this paper, the illustrated uncertainties associated with J_v (and J_{ws}) and J_w are 1% and 5%, respectively. They are subjective estimates, supported by considerations of reproducibility.

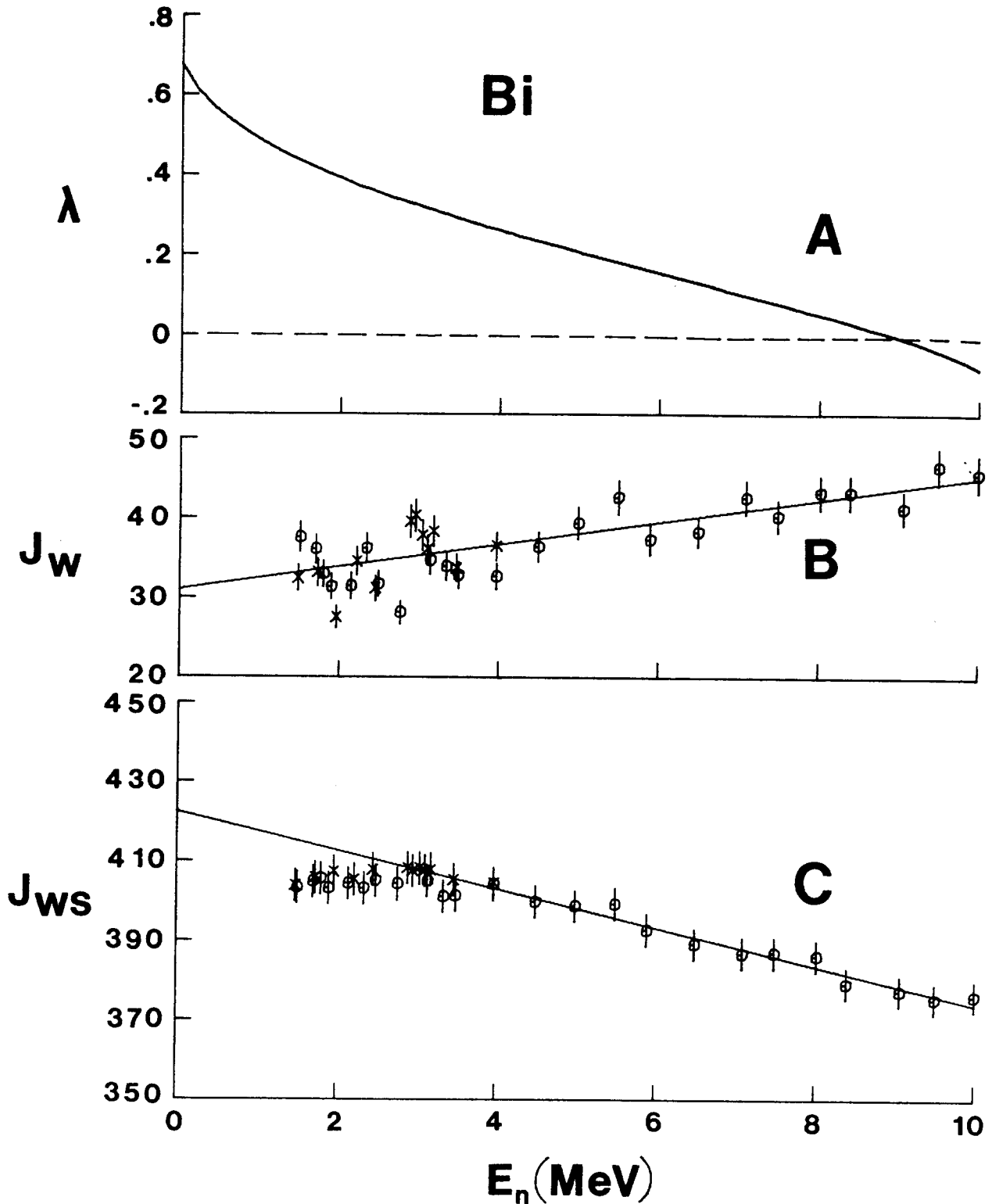


Fig. 6. Part (A), the quantity $\lambda(E)$, related to the strength of the surface-peaked real potential as per Eq. 8 of the text, is shown as a function of laboratory energy. Parts (B) and (C) show the energy variation of the volume integral per nucleon (in $\text{MeV}\cdot\text{fm}^3$) of the surface-peaked imaginary interaction, J_w , and the real Woods-Saxon potential, J_{ws} , respectively, for the model described in Sec. IV-B of the text. The solid curves indicate the best fit to the 4.5 to 10.0 MeV data, Eq. 11. The data symbols have the same connotation as in Fig. 5.

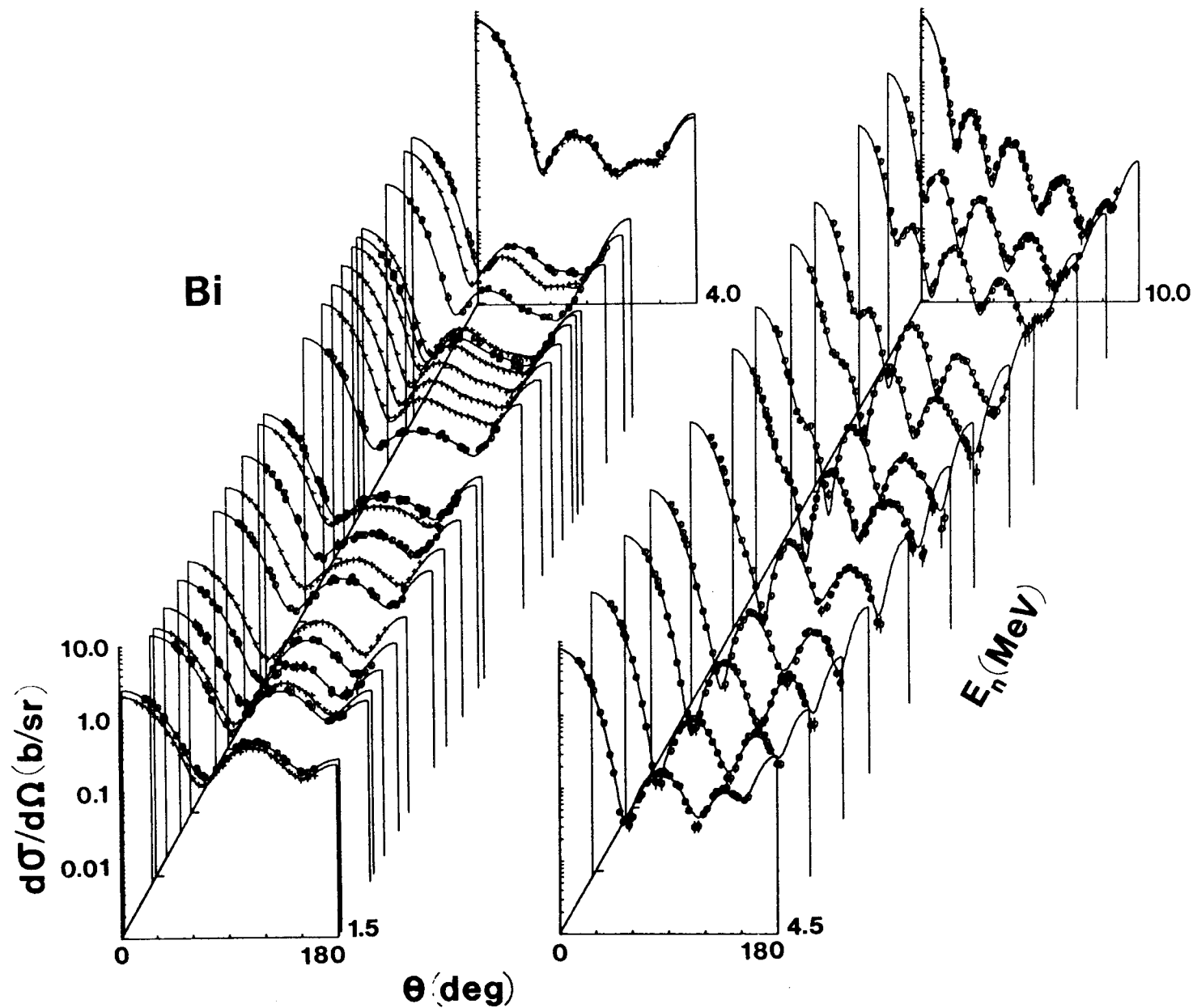


Fig. 7. Comparison of measured values ("o" indicating the present work and that of ref. 5, and "+" that of ref. 6) and the results calculated with the surface-peaked potential described in Sec. IV-B of the text (curves).

V. DISCUSSION

As discussed in the previous section, the level-density parameters, E_0 and T of Eq. 2, were chosen to give a good description of back-angle scattering in the 3.2 to 6.5 MeV range. Since these parameters largely determine the levels sharing in the reaction cross section, it is expected that the predicted inelastic excitation of the first two levels at 897 keV ($7/2^-$) and 1.608 MeV ($13/2^+$) would be sensitive to these quantities. With the values of Eq. 2, the predicted cross sections for the excitation of these two states at, for example, 5.0 MeV incident energy are 110 and 77 mb, respectively, using the conventional optical model of Section IV-A. The values change by $\leq 1.5\%$ if the surface-peaked model of Section IV-B is used. These predictions are in good agreement with the measured values reported by Annand et al. (9). If T changes by $\pm 10\%$ the predicted inelastic cross sections are changed by approximately $\pm 25\%$. On the other hand, the results are less sensitive to changes in E_0 , where a ± 0.1 MeV change alters the predicted inelastic cross sections by approximately $\pm 5\%$. Thus the combination of fitting the back-angle minima of the elastic-scattering cross section and correct prediction of the inelastic excitation of the $7/2^-$ and $13/2^+$ levels puts stringent restrictions on the allowable values of the nuclear temperature, T .

In our calculations, the spin-orbit interaction was estimated from considerations of the 9.0 to 10.0 MeV elastic-scattering angular distributions using the conventional optical model. The resulting spin-orbit parameters, Eq. 4, were then held fixed for the subsequent interpretations of Section IV. Since the predicted neutron polarization depends on the spin-orbit strength, it is of interest to see that Eq. 4 gives the correct magnitude of this quantity. The polarization was calculated at 7.75 MeV using both the conventional (Eqs. 4, 5 and 6) and surface-peaked (Eqs. 4, 8, 10 and 11) models and compared with experimental results of Bulski et al. (28). Either model gave a satisfactory description of the experimental values.

In both models the geometries of the real and imaginary potentials are energy dependent, as given by Eqs. 5 and 10. For the real potential, r_v decreases with increasing energy and this

energy dependence is particularly strong when the conventional model is used. For both models, r_v is relatively large (≈ 1.3 fm) at low energies compared to values resulting from the interpretation of higher-energy data. This dichotomy between r_v values deduced from low- and high-energy interpretations is frequently evident in the literature, and is consistent with the energy-dependent r_v values of the present interpretations. On the other hand, the diffuseness of the real Woods-Saxon potential, a_v , is energy independent for the surface-peaked model and exhibits only a small (if significant) increase with energy for the conventional model. The imaginary potentials in the two cases are quite similar, as one would expect since the surface-peaked term of Section IV-B effects only the real interaction. The imaginary radii, r_w , are almost identical and energy independent. However, the imaginary diffuseness, a_w , rapidly increases with energy, going from almost the delta-function value ($a_w \rightarrow 0$) near zero energy to $a_w = 0.6$ and 0.549 fm at 10.0 MeV for the conventional and surface-peaked models, respectively. Thus, by 8.0 to 10.0 MeV the imaginary diffusenesses have values similar to those usually given by global analyses (29), but at low energies the diffusenesses are quite small, as reported in earlier studies of this nucleus (5, 9).

As can be seen from Eq. 6, the volume-integral-per-nucleon of the real potential decreases with increasing energy for the conventional model. The decrease for ^{209}Bi is much more rapid than it is in the $A = 90$ region (25, 30), and as given in global representations (29). The Woods-Saxon portion of the real surface-peaked potential, Eq. 11, also decreases with energy, with a slope approximately half that deduced from the conventional model. This is to be compared to the energy-independent value found for this quantity in an analysis of neutron elastic scattering from yttrium (25). For both models, the volume-integral-per-nucleon of the imaginary potential is small, a characteristic of nuclei near closed shells (31), and exhibits a modest increase in value with energy.

In order to check the extrapolation of these potentials to very low energies, Eqs. 5, 6, 10 and 11 were used to obtain the parameters for calculating the S-wave strength function. The predicted values of S_0 are 1.345×10^{-4} and 1.195×10^{-4} , for the conventional and surface-peaked models, respectively, compared to

the experimentally deduced value of $(0.65 \pm 0.15) \times 10^{-4}$ (32). Since (33)

$$S_0 \approx \int W(r) |u(r)|^2 dr, \quad (12)$$

where $u(r)$ is the nucleon wave function in the complex well and $W(r)$ the imaginary interaction, it is clear that a smaller value of S_0 can be obtained if either W_0 , the strength of the potential, or a_w , the imaginary diffuseness is changed. For the conventional model, Eqs. 5 and 6 lead to $W_0 = 46.58$ MeV and $a_w = 0.05$ fm at $E = 0$. If a_w is halved, the predicted S_0 is 0.710×10^{-4} . Alternatively, halving W_0 leads to essentially the same result. A similar sensitivity of S_0 was found for the surface-peaked model. Thus, to obtain a good description of the experimentally-deduced S-wave strength function, the zero-energy intercept of J_w must be reduced by about a factor of two. An inspection of Figs. 5 and 6 shows that below 3.0 MeV the values of J_w extracted from a fit to the data of either ref. 5 or 6 seem to "oscillate" about the linear curves given by Eqs. 6 and 11, and this oscillation will probably become even more pronounced as one goes toward zero energy (i.e., fluctuations will become more important). Thus a zero-energy value of J_w , different from the linear extrapolation, would not be surprising.

Each of the models presented in Section IV will now be discussed in detail in order to examine to what extent they throw light on the Fermi Surface Anomaly.

A. Conventional Model

As can be seen from Fig. 5, the 3.0 to 10.0 MeV values of J_v , extracted from our fit to the ^{209}Bi data, lie on a straight line with a slope considerably larger than obtained by Rapaport (29) in his global analysis of 7.0 to 30.0 MeV neutron data. Below 3.0 MeV the J_v values fall consistently below the solid curve, Eq. 6, which illustrates the fit to the 4.5 to 10.0 MeV data. Furthermore, even with a best fit to all the ^{209}Bi J_v values, namely the formula

$$J_v = (454.18 \pm 1.07) - (8.80 \pm 0.21) \times E \text{ MeV-fm}^3, \quad (13)$$

the low-energy values still fall below the curve. This deviation from linearity is small ($\leq 2\%$ at 1.5 MeV), and occurs in an energy region where compound-elastic scattering significantly influences the choice of model parameters. The present interpretation uses the Hauser-Feshbach theory (21), with the most recent Moldauer formulation of width-fluctuation and correlation corrections (22). Detailed numerical studies by Moldauer (22) showed that this correction procedure is equivalent to that of Tepel et al. (34), and Annand et al. (9) show that both give results in this mass-energy region very similar to those obtained with the correction procedures of Hofmann et al. (35). Throughout the above interpretation the channel degree-of-freedom, (ν), calculated from the expression of reference 22 is used. Other values of ν , ranging from 0.5 to 3.0 were examined at the lower energies with small affect on the interpretation (i.e., J_v changed by $\leq 1\%$). However, there is a haunting concern for the validity of the theoretical description at the lower energies. It would be interesting to reinterpret the above data using alternate formulations of statistical-reaction theory (e.g., as described by Zirnbauer (36)), but the means to investigate such new concepts were not available to the authors. The bismuth total cross sections are known to fluctuate by considerable amounts to well over 2.0 MeV (37), and it is reasonable to expect an enhancement of these fluctuations in the elastic channel. Their magnitude and spacing is such that it is not clear whether the observed lower-energy differential-elastic-scattering cross sections, even with the relatively coarse experimental resolutions involved, truly represent an energy-averaged behavior consistent with the optical-model concept. This concern is somewhat mitigated by the good agreement between the 1.5 to 4.0 MeV results of reference 5, which are generally averages over 200 keV intervals, and the "monoenergetic" distributions of reference 6 in the same energy range. However, a close inspection of Fig. 5, while showing no visible sign of fluctuations in the J_v values, suggests that there are fluctuations in the J_w values at lower energies. Moreover, these variations of J_w with energy, following from the independent experimental values of references 5 and 6, tend to be very similar.

Although the ^{209}Bi data seem to result in a small decrease in the absolute value of dJ_v/dE as one goes below 3.0 MeV, the above arguments show how difficult it is to make a definitive statement about this point from a study of low-energy neutron-scattering data alone. On the other hand, the bound-state data do show that dJ_v/dE becomes small, and perhaps even changes sign, for $E < 0$. If one uses the spin-orbit strength of Eq. 4, the $E = 0$ geometry of Eq. 5 for the Woods-Saxon potential, and adjusts the well depth to reproduce the binding energies (38, 39) of the seven known single-particle and six hole states, one finds that the average value of J_v for the former is 438.7 MeV-fm^3 , and 433.8 MeV-fm^3 for the hole states. Thus the most one can say is that the tendency for the J_v values obtained from neutron scattering to level off below 3.0 MeV is consistent with the results needed to give the correct bound-state energies.

In a similar study to that just described, Annand et al. (9) combined data for ^{208}Pb and ^{209}Bi to examine the behavior of J_v over a wide energy range. From a detailed fit to their 6.0, 6.5, and 7.0 MeV data, and to the 20.0, 22.0 and 24.0 MeV ^{208}Pb results of Finlay et al. (40), they concluded that the geometrical parameters of the real and imaginary wells in the 0 to 24.0 MeV incident-energy range should be

$$\begin{aligned}
 r_v &= (1.302 - 0.0055 \times E) \text{ fm} \\
 a_v &= 0.7 \text{ fm} \\
 r_w &= (1.363 - 0.0042 \times E) \text{ fm} \\
 a_w &= (0.162 + 0.0189 \times E) \text{ fm},
 \end{aligned}
 \tag{14}$$

where E is the neutron energy in MeV. With these parameters, and the spin-orbit parameters fixed at $V_{so} = 6.2 \text{ MeV}$, $r_{so} = 1.01 \text{ fm}$ and $a_{so} = 0.75 \text{ fm}$, two-parameter fits, varying V_0 and W_0 , were made to the ^{208}Pb and ^{209}Bi data. For energies greater than 3.0 MeV, they found that J_v decreased with energy with $dJ_v/dE = -4.9 \text{ MeV-fm}^3$. However, below 3.0 MeV, their analysis of the data of reference 6 indicated that dJ_v/dE changed sign (i.e., at 2.961, 2.451, 1.962, and 1.475 MeV the respective J_v values were 420.8, 419.4, 417.1 415.4 MeV-fm^3). On the other hand, our

analysis of the same data ("+"s of Fig. 5) showed that dJ_v/dE is still negative at low energies, but somewhat less so than given by Eq. 6. Because of its implication with respect to the Fermi Surface Anomaly, we examined this point carefully and found that when our potential geometry, Eq. 5, was used, instead of that of Eq. 14, a much better fit to the low-energy data of reference 6 was obtained. Quantitatively, if $\delta\sigma_{\text{exp}}(\theta_1)$ of Eq. 3 is taken to be an angle-independent constant, α , times $\sigma_{\text{exp}}(\theta_1)$, the value of χ^2 per degree of freedom with the geometry of Eq. 5 is always at least a factor of two smaller than that obtained with the geometry of Eq. 14, and this factor increases with decreasing energy, reaching a value of 7.7 at the lowest energy. Thus the behavior of J_v at the low energies is critically effected by the geometry used in the analysis of the data. Furthermore, if the spin-orbit interaction of reference 9, together with the $E = 0$ geometry given by Eq. 14, is used to deduce the values of J_v needed to give the correct particle- and hole-state binding energies, one finds that the average value for the particle states is $J_v = 432.4 \text{ MeV-fm}^3$ and that for the hole states 426.8 MeV-fm^3 . In other words, dJ_v/dE must once again change sign in the region $E \approx -3.0$ to $+1.5$ MeV in order to accommodate the bound-state data. Such an extra "flip" is not theoretically expected. Alternatively, to avoid this second change of sign, the Woods-Saxon well radius for bound states must be smaller than the $E = 0$ limit of Eq. 14 and such an affect has recently been suggested by Mahaux and Sartor (41).

Next, consideration is given to the extrapolation of the conventional model, described by Eqs. 4, 5, 9 and 13, to energies outside the 1.5 to 10.0 MeV range used in its derivation. Although the model gives too large an S-wave strength function, in the few-hundred-keV region it gives as good a prediction of the total cross section as one can reasonably expect in that highly fluctuating domain. This is illustrated by the "x"s in Fig. 8. However, above ≈ 10.0 MeV the rapid energy variation of the geometric parameters, Eq. 5, quickly leads one into difficulty. On the other hand, since $((N-Z)/A)$ is almost the same for ^{208}Pb and ^{209}Bi , it is reasonable to expect the real potential for these two nuclei to be quite similar. (If one uses Rapaport's global parameters (29) the two well depths should only differ by 132 keV.) Furthermore, although the imaginary potentials in the two cases may be quite different at low energies, by the time one reaches 10.0 MeV this difference should

have largely disappeared. Thus, the analysis of the ^{208}Pb data should provide potentials appropriate for the calculation of at least the total ^{209}Bi neutron cross sections at higher energies and to examine the energy dependence of J_V .

In a recent paper, Mahaux and Sartor (42) studied the volume-integral-per-nucleon of the real potential for ^{208}Pb over the energy range 4.0 to 40.0 MeV by fitting a quadratic function of the energy to 23 experimental values. Since here the interest is in a potential valid for $E \geq 10.0$ MeV, the calculation was repeated using the 15 values they considered appropriate in the 9.0 to 40.0 MeV region. With this calculation one finds

$$J_V = (402.6 - 2.35 \times E - 0.0105 \times E^2) \text{ MeV-fm}^3. \quad (15)$$

At 10.0 MeV $dJ_V/dE = -2.56 \text{ fm}^3$ -- a value quite similar to that found by Rapaport (29) in his global analysis of 7.0 to 30.0 MeV neutron data. On the other hand, the Mahaux and Sartor analysis (42), which added only eight additional J_V values in the 4.0 to 7.0 MeV range, gives a much larger slope at 10.0 MeV ($dJ_V/dE = -3.67 \text{ fm}^3$). The fact that the addition of these eight values can change the slope by such a large amount indicates that dJ_V/dE for the low-energy ^{208}Pb data is much larger in magnitude than that needed to fit the high-energy results. The present ^{209}Bi analysis supports this finding since it, too, leads to a rather large value of dJ_V/dE below 10.0 MeV.

Thus, to predict the ^{209}Bi total cross sections at energies ≥ 10.0 MeV it is appropriate to deduce the parameters of the requisite optical model from the same data that led to Eq. 15. Assuming at most a quadratic energy dependence, a least-square fit to the data yields

$$\begin{aligned} V_0 &= (44.634 + 0.106 \times E - 4.763 \times 10^{-3} \times E^2) \text{ MeV} \\ r_V &= (1.2311 - 8.039 \times 10^{-4} \times E - 3.670 \times 10^{-5} \times E^2) \text{ fm} \\ a_V &= (0.7658 - 6.864 \times 10^{-3} \times E + 1.634 \times 10^{-4} \times E^2) \text{ fm} \end{aligned} \quad (16)$$

$$J_w = (39.985 + 1.498 \times E - 6.337 \times 10^{-2} \times E^2) \text{ MeV-fm}^3 \quad (17)$$

$$W_o = (5.780 + 0.109 \times E - 6.430 \times 10^{-3} \times E^2) \text{ MeV}$$

$$r_w = (1.470 - 2.569 \times 10^{-2} \times E + 6.627 \times 10^{-4} \times E^2) \text{ fm}$$

$$a_w = (0.4442 + 1.704 \times 10^{-2} \times E - 3.498 \times 10^{-4} \times E^2) \text{ fm}, \quad (18)$$

where E is the incident energy in MeV. The geometric parameters of this optical potential intersect those of our 1.5 to 10.0 MeV analysis, Eq. 5, at $E = 7.86, 7.78, 8.89$ and 9.55 MeV for $r_v, r_w, a_v,$ and $a_w,$ respectively. Furthermore, the value of J_v obtained from Eq. 15 becomes equal to that given by Eq. 13 in this same energy region (i.e., $E = 8.10$ MeV). It is only the imaginary strengths, $J_w,$ that intersect outside the 8.0 to 10.0 MeV energy range, and then not by much. Eqs. 9 and 17 become equal at 13.0 MeV. If one neglects this latter result, it appears that the transition between the present lower-energy potential and the high-energy ^{208}Pb one takes place in the 8.0 to 10.0 MeV energy range, and clearly a change in slope of the J_v vs E curve is indicated.

If one uses the potentials of Eqs. 16 and 18, together with the spin-orbit interaction of Eq. 4, a rather inferior description of the present 8.03 MeV experimental results is obtained. However, Eqs. 4, 16 and 18 provide a result quite comparable with that shown in Fig. 4 for the present 10.0 MeV data. Furthermore, the optical model described by these equations leads to predicted ^{209}Bi total cross sections in the 10.0 to 20.0 MeV range that are always within 2% of the experimental values (43,44), as indicated by the "x"s in Fig. 8. Thus an excellent fit to the total cross section data can be obtained from a few-hundred keV to 10 MeV using the potential described by Eqs. 4, 5, 9, and 13. The largest differences between measured and calculated values occur near 3.0 MeV where there appears to be some residual fluctuation in the experimental values. In addition, the observed elastic-scattering angular distributions are very well represented, as shown in Fig. 4. Making the transition to the higher-energy model of Eqs. 16 and 18, one extends the good representation of the total cross section to 20.0 MeV. Further extrapolation to higher energies is doubtful because Eq. 18 contains no volume absorption, which becomes important at higher energies.

B. Surface-Peaked Real Potential

Fig. 9 shows the total volume-integral-per-nucleon of the real potential, J_v , which is the sum of the Woods-Saxon part, J_{ws} , and the surface component, $\lambda(E)J_w$, where $\lambda(E)$, J_{ws} and J_w are shown in Fig. 6. Assuming a linear energy dependence, a best fit to the 4.5 to 10.0 MeV data gives

$$J_v = ((442.50 \pm 2.57) - (7.27 \pm 0.34) \times E) \text{ MeV-fm}^3. \quad (19)$$

Again, the data for $E \geq 3.0$ MeV are well represented by this straight line, but below ≈ 3.0 MeV the J_v values resulting from this fit lie consistently below the predictions of Eq. 19. In the conventional model the deviation of the lowest-energy points from the straight line given by Eq. 6 was $\leq 2\%$, while in this case the discrepancy is somewhat larger ($\leq 3\%$). If a linear fit is made to all of the data one finds

$$J_v = ((432.27 \pm 1.18) - (5.89 \pm 0.23) \times E) \text{ MeV-fm}^3. \quad (20)$$

Even with this fit, indicated by the "b" line in Fig. 9, the experimentally-derived values lie below the linear curve for $E \leq 2.5$ MeV, but now the discrepancy is at the 1% level. Thus, again, it is hard to support a definitive deviation from linearity of J_v from a study of the 1.5 to 10.0 MeV neutron-scattering data.

The values of J_v needed to give the correct binding energies for the seven known single-particle states and the six hole states in ^{208}Pb (38, 39) are shown in Fig. 9. In carrying out these calculations it was assumed that the geometry of the surfaced-peaked real potential is given by the $E = 0$ limit of Eq. 10. The values of $\lambda(E)$ and J_w were computed, for these negative energies, from the principal-value integral of Eq. 8 and with the assumption that J_w is a quadratic function of $(E - E_F)$ near the Fermi surface, E_F , i. e.,

$$J_w = (0.969 (E + 5.65)^2) \text{ MeV-fm}^3. \quad (21)$$

With this part of the potential fixed, the Woods-Saxon well depth

was varied so as to reproduce the observed binding energies. Two calculations were carried out:

- a) r_v and ϵ_1 were held fixed at the zero-energy values given by Eq. 21. The results for J_v in this case are shown by "o"s in Fig. 9.
- b) a_v was held fixed at 0.68 fm and r_v given the energy dependence found from the fit to the neutron-scattering data, Eq. 10. The resulting J_v values are indicated by "x"s in Fig. 9.

Clearly, for either calculation, the bound-state data give rise to J_v values that fall much below the straight-line extrapolations of either Eqs. 19 or 20. Furthermore, J_v for the single-particle states is only slightly larger than the $J_v \approx 420$ MeV-fm³ value found at the lowest neutron energies. In case a), the the average value of J_v for the single-particle states is 425.7 MeV-fm³, with an rms deviation of ± 6.7 MeV-fm³, while in case b) the value and rms deviation are 432.0 MeV-fm³ and ± 7.4 MeV-fm³.

Fig. 9 shows a semi-theoretical estimate of J_v ,

$$J_v = J_{ws} + \lambda(E)J_w, \quad (22)$$

obtained when $\lambda(E)$ is given by the principal-value integral of Eq. 8, and J_w is given by Eq. 9 for $E \geq 0$ and by Eq. 21 for $-11.0 \leq E \leq 0$ MeV. Two possibilities for J_{ws} were considered: first, that for all energies involved

$$J_{ws} = (415.08 - 3.81 \times E) \text{ MeV-fm}^3, \quad (23)$$

which is the best fit to all the neutron-scattering data, and second, that J_{ws} has the form of Eq. 23 for $E \geq 0$ and is 415.08 MeV-fm³ for all $E \leq 0$. For $E \geq 0$ the predicted values of J_v are identical in the two cases, and are almost the same as the values given by either Eq. 19 or 20 for $E \geq 1.5$ MeV. For $E < 0$, the

lower curve, which corresponds to a constant J_{ws} , comes quite close to the J_v values needed to give the correct binding energies when a_v and r_v are energy independent (calculation "a" of the above paragraph). On the other hand, when J_{ws} is given by Eq. 23 the predicted values of J_v for $E < 0$ are similar to those obtained for the bound states when the radius of the Woods-Saxon well has an energy dependence (calculation "b", above). Thus, over the range -11.0 to $+10.0$ MeV the energy dependence of J_v predicted by Eq. 22 is quite close to that needed to fit the experimental data. If an energy-dependent geometry is used in the bound-state calculation, J_{ws} should also be energy dependent and have the form given in Eq. 23. However, when the bound-state-well geometry is energy independent so is J_{ws} for $E < 0$, and it has the value given by Eq. 23 with $E = 0$. For either calculation, the point at which $dJ_v/dE = 0$ is predicted to occur at a negative energy.

As already mentioned, the use of the model described by Eqs. 4, 8, 10, and 11 leads to an S-wave strength function that is a factor of two larger than deduced from resonance measurements. On the other hand, a reasonable description of the neutron total cross section is achieved down to at least 500 keV using this model. A result somewhat closer to experiment can be obtained if one uses J_{ws} given by Eq. 23, together with the best fit to all the J_w values shown in Fig. 6B,

$$J_w = ((29.53 \pm 0.97) + (1.58 \pm 0.23) \times E) \text{ MeV-fm}^3. \quad (24)$$

When these strengths are used, in conjunction with the geometry of Eq. 10, the predicted total cross section is shown by the "•" symbols in Fig. 8.

In order to evaluate the strength of the surface real potential, $\lambda(E)$ of Eq. 8, it was necessary to know the form of $W(r,E)$ at all energies. Since first-hand knowledge of $W(r,E)$ extended only to 10 MeV, it was assumed that for $E > 10.0$ MeV the surface imaginary potential of Walter and Guss (27) was appropriate. Thus, inherent in the present model is the assumption that above 10.0 MeV neither the imaginary strength given by Eq. 11 or 24 is appropriate, but instead the parameters of the surface-imaginary potential are:

$$\begin{aligned}
 W_0 &= (7.776 - 0.157 \times E) \text{ MeV} \\
 r_w &= 1.282 \text{ fm} \\
 a_w &= 0.512 \text{ fm.}
 \end{aligned}
 \tag{25}$$

Extrapolation of the present model above 10.0 MeV implies that one should use the surface absorption of Eq. 25, the value of $\lambda(E)$ calculated from Eq. 8, and a real Woods-Saxon well with the geometry of Eq. 10 and the strength of Eq. 23. When this is combined with the volume absorption of the Walter and Guss potential, the result is a poor fit to the total-cross-section data above ≈ 10.0 MeV. For example, at 12.0 MeV the calculated value falls 5.7% below the measured one, and at 20.0 MeV it is 5.9% too small. On the other hand, if one does not worry about self consistency and instead calculates the value of $\lambda(E)$, assuming the Walter and Guss interaction, and then uses that value in conjunction with the geometry and strength of the imaginary potential given by Eqs. 10 and 24, a good description (within $\approx 2\%$) of the total cross section is obtained up to 17.5 MeV. Furthermore, a suitable description of the 11.2 MeV elastic-scattering data of Ferrer et al. (45) is obtained except at four angles ($\approx 110^\circ$, 115° , 150° , and 155°) out of thirty, and even in these instances the differences between calculation and experiment are only a few mb/sr.

When the conventional optical model, discussed in Sections IV-A and V-A, is used to interpret the data, it is possible to show that the description of the high-energy ^{208}Pb experiments, when combined with the lower-energy ^{208}Pb and ^{209}Bi data, implies a change in dJ_v/dE in the neighborhood of 10.0 MeV.

Although several analyses of high-energy ^{208}Pb data have been made (9,40) using the real surface-peaked potential model, they cannot be easily connected with the present treatment of the ^{209}Bi data because of the differences in the way $\lambda(E)$, Eq. 8, was calculated. As suggested by Mahaux and Ngô (3), J_w in the present analysis was assumed to be symmetric about the Fermi energy, E_F , and as a consequence a substantial negative contribution to the dispersion integral is obtained from values of $E' < 0$. This causes $\lambda(E)$ to change sign at approximately 9.0 MeV in the present model. However, in the work of Annand et al. (9) only the contribution to the principal-value integral for $E' > 0$ was included. Implicitly they assumed that $W(r, E')$ dropped discontinuously to zero for $E' \leq 0$, which not only leads

to a discontinuity in $\lambda(E)$ at $E = 0$ but also has the consequence that $\lambda(E)$ does not get the large negative contribution from the principal-value integral. Therefore, their $\lambda(E)$ goes through zero at a much higher energy than ours (≈ 20.0 MeV). In the analysis of Finlay et al. (40), the strength of the surface real potential was taken to be 0.24 times the value calculated by Ahmad and Haider (46). These latter authors used the surface absorption potential appropriate for proton scattering from ^{40}Ca , and assumed $W(r, E')$ went to zero at $E' = 0$. $\lambda(E)$ calculated in this way changes sign at approximately 30.0 MeV. Moreover, the data for ^{40}Ca cannot be used in a self-consistent description of ^{208}Pb . Thus, until one has calculations for both ^{209}Bi and the high energy ^{208}Pb data that use the same ground rules for evaluating $\lambda(E)$, it is not possible to demonstrate a change in the magnitude of dJ_v/dE in the 10.0 MeV region from an analysis of the neutron-scattering data using the surface-peaked real-potential model.

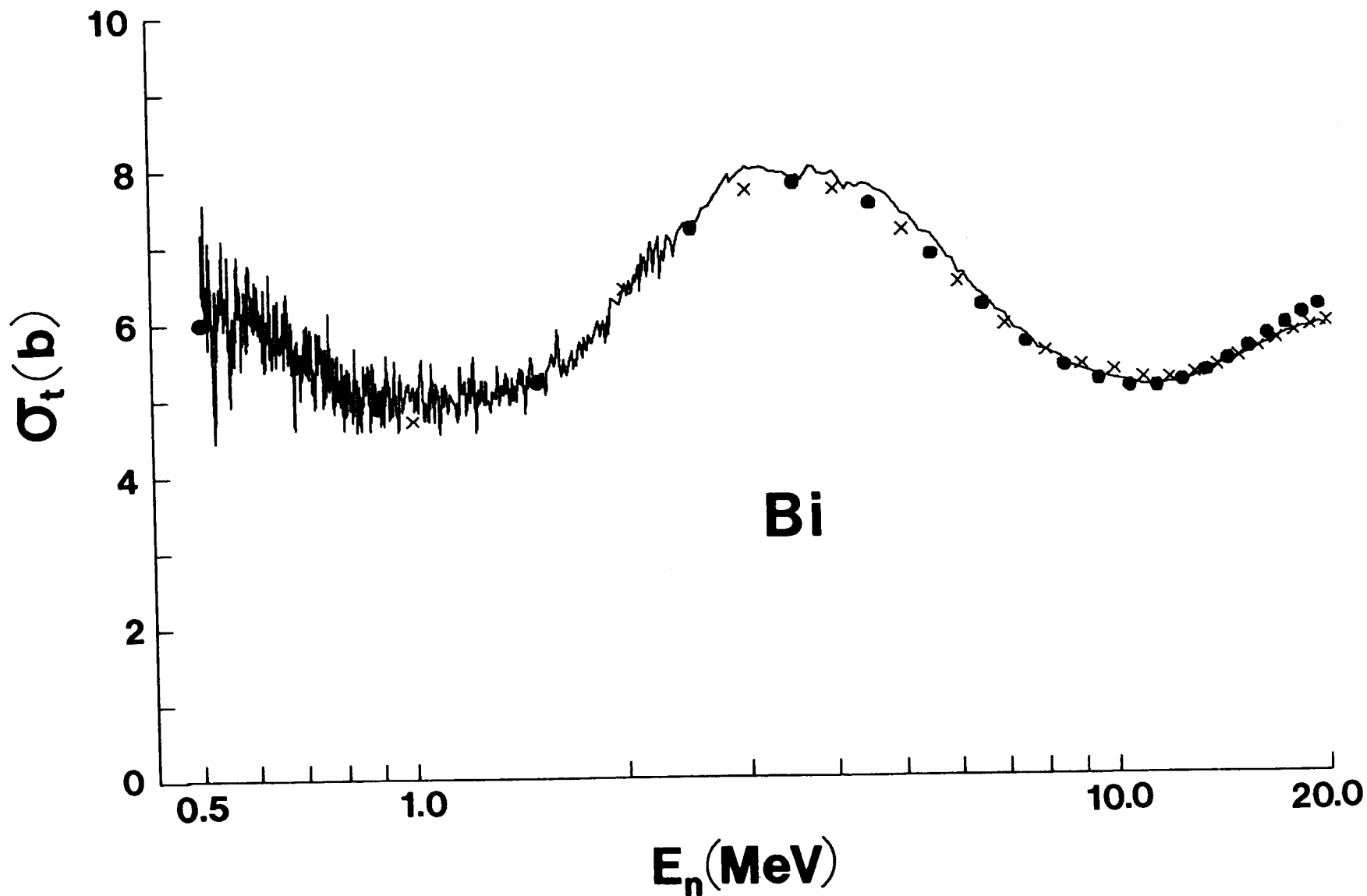


Fig. 8. Comparisons of measured and calculated neutron total cross sections of bismuth. The solid curve indicates the experimentally-based evaluation of reference 43. The "x"s are the results calculated from the conventional model using Eqs. 4, 5, 9 and 13 below 10.0 MeV and the high-energy description given by Eqs. 4, 16 and 18 above 10.0 MeV. The solid data symbols represent results calculated with the surface-peaked potential of Eqs. 4, 8, 10, 23 and 24 derived from the present interpretation of the elastic-scattering data.

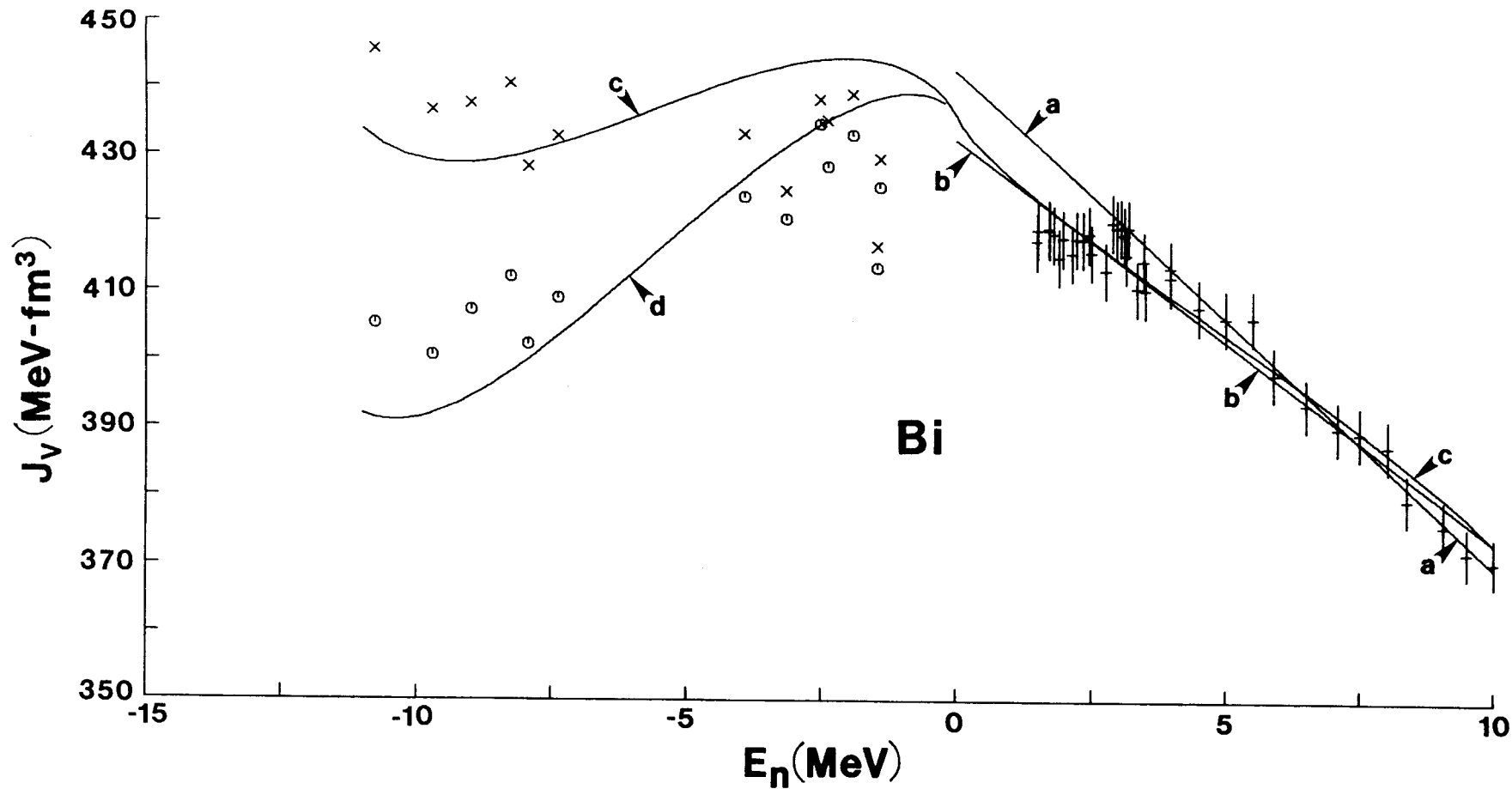


Fig. 9. The values of the total volume-integral-per-nucleon, J_V , (in $\text{MeV}\cdot\text{fm}^3$) of the real potential discussed in Secs. IV-B and V-B of the text. The values at positive energies, "+" symbols, were obtained by fitting the ^{209}Bi elastic-scattering data. Curve "a" is a fit to these results over the 4.5 to 10.0 MeV energy range, Eq. 19, while curve "b" is a fit to all scattered-neutron data, Eq. 20. The negative-energy values were obtained from a fit to the observed binding energies of particle- and hole-states. The states considered, in order of increasing binding energy, were $2d_{3/2}$, $1g_{7/2}$, $3s_{1/2}$, $2d_{5/2}$, $0j_{15/2}$, $0i_{11/2}$, $1g_{9/2}$, $2p_{1/2}$, $1f_{5/2}$, $2p_{3/2}$, $0i_{13/2}$, $1f_{7/2}$, and $0h_{9/2}$. The values denoted by "x" were obtained using a Woods-Saxon well with the energy-dependent geometry of Eq. 10, whereas those shown by "o" were obtained with $a_v = 0.68$ fm and $r_v = 1.28$ fm. Curve "c" is the prediction of Eq. 22 when J_{ws} has the energy dependence of Eq. 23, whereas in curve "d" $J_{ws} = 415.08$ $\text{MeV}\cdot\text{fm}^3$ for negative energies.

VI. SUMMARY

The neutron differential elastic-scattering cross sections of ^{209}Bi were measured from 4.5 to 10.0 MeV at incident neutron energy intervals of ≈ 0.5 MeV and at ≥ 40 scattering angles distributed between $\approx 18^\circ$ and 160° . Resolutions were sufficient to separate the elastically-scattered neutron component from known inelastically-scattered groups. Particular attention was given to the specification of uncertainties necessary for rigorous fitting of the data to obtain model parameters. The present experimental results were combined with the lower-energy distributions previously reported from this laboratory (5), and with those reported by Olsson et al. (6), to obtain a comprehensive experimental elastic-scattering data base extending from ≈ 1.5 to 10.0 MeV. This data base was interpreted in terms of the spherical optical-statistical model with and without the surface-peaked component of the real potential required by the dispersion relation (2). The main conclusions reached from these analyses were:

1) Properties of the real optical-model potential

In order to fit the ^{209}Bi data over the 1.5 to 10.0 MeV energy range, the radius of the Woods-Saxon well, r_v , used for the volume part of the potential must decrease with increasing energy. In the case of the conventional analysis, described in Section IV-A, this decrease is quite strong (see Eq. 5). When the surface-peaked real potential is added, the decrease in r_v with increasing energy remains, but is much less as can be seen from a comparison of Eqs. 5 and 10. For both models the diffuseness of the real well can be taken to be energy independent, although a slight improvement in the fit to the data with the conventional model was obtained when the slow energy dependence of Eq. 5 was used. The volume integral of the Woods-Saxon potential, J_{ws} , of the surface-peaked model of Section IV-B decreases in value as the energy, E , increases, with $dJ_{ws}/dE = -3.81 \text{ fm}^3$ when a best fit to all the data is made. This appreciable slope is to be contrasted with $dJ_{ws}/dE \approx 0$ found in the analysis of the yttrium data (25). The total volume-integral-per-nucleon of the real potential, J_v , decreases with increasing energy, the slope depending slightly upon the model used in the analysis of the data (compare Eqs. 13 and 20).

Over the energy range 3.0 to 10.0 MeV, for either model, this slope was constant. Below 3.0 MeV, dJ_v/dE seems to decrease in magnitude as shown in Figs. 5 and 9, but it remains negative to at least 1.5 MeV. It is far from clear that this low-energy behavior of J_v , deduced from neutron-scattering data alone, is a manifestation of the Fermi Surface Anomaly as the effect is marginal and there remain concerns for the fluctuations and the interpretation of the compound-nucleus process that is a significant consideration at these low energies.

ii) Properties of the imaginary optical-model potential

Below 10.0 MeV the imaginary interaction was described by a Woods-Saxon-derivative well. No evidence for volume absorption was found. The behavior of the imaginary interaction was similar for both the conventional and surface-peaked models described in Sections IV-A and IV-B. The potential radius was energy independent. On the other hand, the diffuseness varied rapidly with energy as can be seen from Eqs. 5 and 10. Near zero energy the imaginary potential approaches a delta function, whereas in the 8.0 to 10.0 MeV region it displays a diffuseness characteristic of that found in a global analysis of neutron-scattering data (29). J_w , the volume-integral-per-nucleon of the imaginary potential, is small, as is characteristic of nuclei near closed shells (31), and it increases slightly with increasing energy. Below 3.0 MeV, the J_w values, illustrated in Figs. 5 and 6B, exhibit some scatter which may be a manifestation of residual compound-nucleus fluctuations.

iii) Fermi Surface Anomaly

According to Mahaux and Ngô (3), the total volume-integral-per-nucleon of the real potential, J_v , should have a slope $dJ_v/dE = 0$ at approximately 4.0 MeV incident neutron energy. Our analyses of the ^{209}Bi data show that between 3.0 and 10.0 MeV dJ_v/dE is constant and has a value between -6.0 fm^3 and -9.0 fm^3 , depending upon which model is used to analyze the data. Below 3.0 MeV, dJ_v/dE seems to decrease in magnitude, and this is consistent with the values of J_v needed to give the correct binding energies of single-particle and single-hole states, as shown in Fig. 9. However, the point where $dJ_v/dE = 0$,

predicted by the use of Eq. 22, occurs at negative energies. Annand et al. (9) analyzed some of the same low-energy neutron-scattering data used in the present interpretations (that of reference 6) and reported a change in sign of dJ_v/dE at positive energies below 3.0 MeV. The present analysis of the same data, resulting in considerably better fits to the measured values, indicated a reduction of dJ_v/dE below 3.0 MeV but no change of sign. Thus it seems that the only solid evidence for the Fermi Surface Anomaly at low (and negative) energies rests on considerations of the bound states.

iv) J_v vs E Curve near 10.0 MeV.

As noted above, the present analyses of the ^{209}Bi data below 10.0 MeV results in large values of dJ_v/dE , -6.0 to -9.0 fm^3 depending on the model used. On the other hand, a fit to all the ^{208}Pb data above 9.0 MeV, similar to that carried out by Mahaux and Sartor (42), leads to $dJ_v/dE \approx -2.6 \text{ fm}^3$ at $E_n \approx 10.0$ MeV. This latter value is quite close to the global value, $dJ_v/dE = -2.28 \text{ fm}^3$, reported by Rapaport (29) from an analysis of 7.0 to 30.0 MeV neutron-scattering data. By combining the ≤ 10.0 MeV ^{209}Bi and ≥ 10.0 MeV ^{208}Pb results, it is clear that in the vicinity of 10.0 MeV dJ_v/dE makes a transition from a relatively large negative slope to a smaller negative value characteristic of higher-energy interpretations. Furthermore, as discussed in Section V-A, the geometrical parameters of the low-energy ^{209}Bi potential become equal to those of the high-energy ^{208}Pb potential in the same energy range. If one carefully examines the calculational results of Mahaux and Ngô (3), one sees that they predict a change of this nature in the region of 15.0 MeV incident-neutron energy. The combination of the analyses of the ^{208}Pb and ^{209}Bi data, together with the interpretation of binding energies, leads to an energy dependence of J_v quite similar to that predicted by Mahaux and Ngô (3), but shifted downward in energy by about 5.0 MeV.

v) Low-energy / High-energy Dichotomy

From an analysis of S-wave strength functions and neutron scattering and polarization data at low energies, Moldauer (47) concluded that the absorptive part of optical-model

potential was sharply peaked near the nuclear surface (i.e., a_w was small) and r_v was greater than 1.26 fm for all but the transuranic elements. These results are in marked contrast to the global values, (29) $r_v = 1.198$ fm and $a_w = 0.59$ fm, arising from a fit to the 7-30 MeV neutron-scattering data. The present ^{209}Bi and ^{208}Pb analysis provides another example of this dichotomy. If the low-energy variation of these parameters with energy is rapid whereas the high-energy variation is slight, as found in the present analysis, this has important ramifications with respect to the extrapolation between low- and high-energy optical-model parameters.

ACKNOWLEDGMENTS

The authors are indebted to members of the Applied Nuclear Physics Section, Applied Physics Division, for their assistance in the above work.

REFERENCES

1. J. Blomqvist and S. Wahlborn, Ark. Fys. 16 545 (1960).
2. See for example, G. R. Satchler, Direct Nuclear Reactions Clarendon Press, Oxford (1983).
3. C. Mahaux and H. Ngô, Nucl. Phys. A378 205 (1982); Phys. Lett. 100B 285 (1981).
4. E. Barnard, J. deVilliers, D. Reitmann, A. Smith and J. Whalen, Nucl. Sci. and Eng. 41 63 (1970).
5. P. Guenther, A. Smith and J. Whalen, Nucl. Sci. and Eng., 75 69 (1980).
6. N. Olsson, B. Holmqvist and E. Ramstrom, Nucl. Phys. A385 285 (1983).
7. C. Zafiratos, T. Oliphant, J. Levin and L. Cranberg, Phys. Rev. Lett. 14 913 (1965).
8. B. Holmqvist and T. Wiedling, Aktiebolaget Atomenergi Report, AE-430 (1971).
9. J. Annand, R. Finlay and F. Dietrich, Nucl. Phys. A443 249 (1985).
10. C. Budtz-Jørgensen, P. Guenther, A. Smith, J. Whalen, W. McMurray, M. Renan, and I. van Heerden, Z. Phys. A319 47 (1984).
11. A. Smith, P. Guenther, J. Whalen, I. van Heerden and W. McMurray, J. Phys. G11 125 (1985).
12. A. Smith, P. Guenther, R. Larsen, C. Nelson, P. Walker, and J. Whalen, Nucl. Instr. and Methods 50 277 (1967).
13. M. Drosig, Proc. Advisory Group Mtg. on Neutron Source Properties, Leningrad (1986) IAEA Press, Vienna.
14. A. Smith, P. Guenther and R. Sjoblum, Nucl. Instr. and Methods 140 397 (1977).
15. Nuclear Data Standards for Nuclear Measurements, IAEA Tech. Report 227, Editors, H. Condé, A. Smith and A. Lorenz, IAEA Press Vienna (1983).

16. P. T. Guenther, Elastic and Inelastic Scattering of Fast Neutrons from the Even Isotopes of Tungsten, Thesis, University of Illinois (1977).
17. A. Smith and P. Guenther, Argonne National Laboratory Report, to be published.
18. R. M. Wilenzick, K. K. Seth, P. R. Bevington and H. W. Lewis, Nucl. Phys. 62 511 (1965).
19. J. R. Beyster, M. Walt and E. W. Salmi, Phys. Rev. 104 1319 (1956).
20. P. E. Hodgson, Nuclear Reactions and Nuclear Structure, Clarendon Press, Oxford (1970).
21. W. Hauser and H. Feshbach, Phys. Rev. 87 366 (1952).
22. P. A. Moldauer, Nucl. Phys. A344 185 (1980).
23. Table of Isotopes, 7th edition, Edited by C. M. Lederer and V. S. Shirley, John Wiley and Sons Inc., New York (1978).
24. A. Gilbert and A. Cameron, Can. J. Phys. 43 1446 (1965).
25. R. D. Lawson, P. T. Guenther and A. B. Smith, Phys. Rev. C34 1599 (1986).
26. R. Sartor and C. Mahaux, Phys. Rev. C21 1546 (1980).
27. R. L. Walter and P. P. Guss, Proc. Conf. on Nuclear Data for Basic and Applied Science, Vol. 2, p. 1079, Gordon and Breach, New York (1986).
28. G. Bulski, W. Grum, J. Hammer, H. Postner, G. Schleussner and E. Speller, Proc. Antwerp Conf. on Nucl. Data for Sci. and Technology, p. 783, D. Reidel Pub. Co., Dordrecht, Holland (1982).
29. J. Rapaport, Phys. Reports, 87 25 (1982).
30. A. B. Smith, P. T. Guenther and R. D. Lawson, Nucl. Phys. A455 344 (1986).
31. A. M. Lane, J. Lynn, E. Melkonian and E. Rae, Phys. Rev. Lett. 2 424 (1959); W. Vonach, A. Smith and P. Moldauer, Phys. Lett. 1 331 (1964); A. Smith, P. Guenther and J. Whalen, Nucl. Phys. A415 1 (1984).

32. S. Mughabghab, M. Divadeenam and N. E. Holden, Neutron Cross Sections, Vol. 1, Pt. B, Academic Press, New York (1981).
33. C. E. Porter, Phys. Rev. 100 935 (1955).
34. J. Tepel, H. Hofmann and H. Weidenmuller, Phys. Lett. B49 1 (1974).
35. H. Hofmann, J. Richert, J. Tepel and H. Weidenmuller, Ann. Phys. 90 403 (1975).
36. M. Zirnbauer, Proc. Conf. on Neutron-Nucleus Collisions, A Probe of Nuclear Structure, p-481, Editors, J. Rapaport, R. Finlay, S. Grimes and F. Dietrich, AIP Conf. Proc. No. 124, AIP Press, New York (1985).
37. S. Cierjacks, P. Forti, D. Kopsch, L. Kropp, J. Nebe and H. Unseld, Kernforschung Karlsruhe Report, KFK-1000 (1968).
38. A. H. Wapstra and K. Bos, Atomic Data and Nuclear Data Tables, 19 177 (1977).
39. M. R. Schmorak and R. L. Auble, Nucl. Data. Sheets, B5 205 (1971).
40. R. W. Finlay, J. R. M. Annand, T. S. Cheema, J. Rapaport and F. S. Dietrich, Phys. Rev. C30 796 (1984).
41. C. Mahaux and R. Sartor, Phys. Rev. Lett. 57 3015 (1986).
42. C. Mahaux and R. Sartor, Phys. Rev. C34 2119 (1986).
43. O. Bersillon, B. Caput and C. Philis, Proc. Antwerp Conf. on Nucl. Data for Sci. and Technology, p-665, D. Reidel Pub. Co., Dordrecht, Holland (1982).
44. A. Smith, P. Guenther, D. Smith, J. Whalen and R. Howerton, Argonne National Laboratory Report, ANL/NDM-51 (1980).
45. J. C. Ferrer, J. D. Carlson and J. Rapaport, Nucl. Phys. A275 325 (1977).
46. I. Ahmad and W. Haider, J. Phys. G2 L157 (1976).
47. P. A. Moldauer, Nucl. Phys. 47 65 (1963).